Automating the Diagnosis and Quantification of Urinary Schistosomiasis

Satyajith Jujjavarapu

Master of Science Thesis

TU Delft Delft University of Technology

Delft Center for Systems and Control

Automating the Diagnosis and Quantification of Urinary Schistosomiasis

Master of Science Thesis

For the degree of Master of Science in Embedded Systems at Delft University of Technology

Satyajith Jujjavarapu

February 27, 2020

Faculty of Electrical Engineering, Mathematics and Computer Science (EEMCS) · Delft University of Technology

Delft University of Technology
Department of
Delft Center for Systems and Control (dcsc)

The undersigned hereby certify that they have read and recommend to the Faculty of Electrical Engineering, Mathematics and Computer Science (EEMCS) for acceptance of the thesis entitled

Automating the Diagnosis and Quantification of Urinary Schistosomiasis

by

Satyajith Jujjavarapu

in partial fulfillment of the requirements for the degree of

Master of Science Embedded Systems

Dated: February 27, 2020

Supervisor(s):

prof. dr. G. Vdovine

ir. Temitope E. Agbana

Reader(s):

dr. ir. Diehl, J.C.

dr. C. Smith

Abstract

Schistosomiasis is a neglected tropical disease (NTD) that affects around a quarter-billion people worldwide. Most of the infected people live in tropical regions, especially in sub-Saharan Africa, where there is limited access to diagnostic and other relevant medical facil-ities. The current reference standard diagnostic procedure - conventional microscopy - is a relatively inexpensive procedure to use on a large scale, but it still requires trained operators and an initial financial investment which are hard to procure and maintain in remote areas with inadequate facilities. Moreover, the diagnostic sensitivity of the procedure is modest and varies over a wide range. In this work, we present the development of an inexpensive diagnostic instrument for urinary schistosomiasis that is automated to scan, analyse and di-agnose the disease, and quantify the level of infection. We explore the design of the device with an open-source philosophy in mind, to enable makerspaces and other interested parties to reproduce the device locally. The device is manufacturable for as little as €200. It adheres to the standard sample preparation and diagnosis procedure established by the World Health Organisation (WHO), and images the relevant biomarkers to an adequate resolution for au-tomated detection, diagnosis, and quantification for epidemiological surveillance. We believe this device can be an essential means for point-of-care diagnosis in resource-limited settings.

Table of Contents

List of Figures

List of Tables

Acknowledgements

I want to thank my supervisors, Prof. *Gleb Vdovine* and Ir. *Temitope Agbana* for their enthusiasm, devotion and guidance to this project, and in allowing me to explore and at times stray away from the initially intended line of work. I am grateful to Prof. *Jan Carel Diehl*, from the faculty of Industrial Design Engineering (IDE), TU Delft, for arranging for me to work closely with design engineers, and finding the resources to enable my travel to Nigeria. In the process of working with design engineers, I learned many new skills and worked with a lot of people, many of whom are now my good friends. I wish the three of you all the best for every new adventure you embark on.

I want to thank *G Young Van*, my friend and researcher at IDE, for her swiftness in organising and arranging anything - from materials to meetings - on prompt notice.

To *Salvador Emilio Lluch Sicard*, my good friend and amazing designer, thank you for working with me again to build an improved and polished version of our final design.

To the smartest person I know, my very close friend, *Paulo* (The Adamant) *Cerqueira*, thank you for all the discussions, feedback and comedy. Also, thank you for proof-reading this thesis report. You are a proof-reading machine with no close competition.

This page is probably inadequate to fill in the names of all the people I want to mention. So I say, to all the researchers - technology and design - who worked (are working) on the development of the diagnostic tools, thank you for your amazing effort on this journey. It was a pleasure working with all of you.

Special thanks to Prof. *Michel Verhaegen*, the man who recommended I join this adventure when I was in search of a master's thesis project.

Delft, University of Technology — Satyajith Jujjavarapu
February 27, 2020

Chapter 1

Introduction

This work concerns schistosomiasis, also known by the names *snail fever* and *bilharzia*, which is a disease that is caused by parasitic flatworms called Schistosomes, and their ova. It is one of the most prominent helminth infections (a parasitic worm infection of a specific part of the body) and is listed as a neglected tropical disease (NTD) [8]. Schistosomiasis actively affected around 230 to 252 million people in 2015 [9, 10], which is a significant 23% drop from 2005 [10]. Nonetheless, the number of people infected by the disease is still very high, and it results in many acute and chronic medical conditions which affect an individual's physical and cognitive capacities [9, 11, 1, 12, 13]. It reportedly results in deaths in the wide range of 4.4 to 200 thousand per year [14]. It is estimated that around 600 to 700 million people, living in 70 to 80 countries, are at risk of infection to the disease [11, 13]. Of the people who are infected by it globally, 90% of them live in Africa [11]. It is majorly noticeable in poor and rural communities, mainly agricultural and fishing populations [11] where people are in frequent contact with infested water bodies. The prevalence of schistosomiasis is second only to malaria in Africa [13].

The disease is currently treated by the periodic large-scale distribution of *praziquantel*, the choice of medication, to affected communities [9, 11]. The medication is reported to be effective and inexpensive, but less than 50% of the people who were infected received the treatment in 2016 [15]. The mode of action of the drug is presently not known, and it is reported to be effective only against adult schistosome worms and fares poorly against immature schistosome larvae [9].

Schistosomiasis is of two principal forms: intestinal and urogenital [11]. There are around twenty-five known species of schistosomes, of which five species have been observed to infect humans [9, 11]. In this work, we focus on urogenital schistosomiasis, which is the most prevalent form of schistosomiasis affecting humans [16]. The responsible schistosome is *Schistosoma haematobium* (*S. haematobium*). Evidence suggests that the overall morbidity caused by the infection is due to the schistosome ova, which in large numbers are not excreted and get lodged in the urogenital system [9]. The current reference standard for the diagnosis and for the collection of quantitative data for epidemiological surveillance, is manual microscopic examination of the filtered urine sample for the presence of schistosome ova [9, 11, 1, 16, 17].

Taking into account that the disease is notably prevalent in low- and middle-income countries (LMIC), to speed up the treatment, control and elimination schemes, the scalability of the standard procedure for the examination should be re-evaluated for resource-limited settings. Conventional microscopy, in general, requires hiring microscopists and technicians, is labour-intensive and involves high initial and maintenance costs [18]. Moreover, the performance of the examination procedure relies on the experience and technique of an individual analyst, which can lead to significant discrepancies in parasite identification and quantification [19]. In the long term, these factors will make the performance worse, because localities with light infections and low endemicity will require methods providing relatively higher diagnostic sensitivity and specificity [9, 16, 20].

In the literature, we find reports on various innovations [21, 22, 23] and alternative [9, 16, 24] diagnostic tests for urinary schistosomiasis. A notable factor which forms the basis for these developments is that the production of schistosome ova in the host body begins 5-7 weeks after infection, which eliminates the use of microscopy for early diagnosis or screening [9, 21, 25]. Despite this drawback, microscopy is still the choice of diagnostic method in resource-limited settings, as it is a comparatively inexpensive procedure.

Automating the operation of standard microscopes or the use of digital microscopes can aid in improving the diagnostic sensitivity, but such devices will be expensive. The development of inexpensive and portable optical devices, while providing comparable image quality for diagnosis, integrated with computer vision software, can mitigate the operational drawbacks with conventional microscopy to a great extent. In the scientific literature, we note a rise in research geared towards realizing mobile phone microscopes for diagnosing and quantifying helminth infections [16, 26] and also other parasites, like malaria [27, 28]. Designing economical image acquisition devices integrated with sophisticated object detection models can pave the way for smart diagnostic and mapping devices that are deployable in remote regions.

1-1 Thesis objective

In this thesis, we investigate and design a proof-of-concept instrument to automate the diagnosis and quantify the intensity of infection, of urinary schistosomiasis. The first device iteration is a mobile-phone microscope with a reverse-lens optical setup. The aim was to image the biomarkers - the *S. haematobium* ova - in filtered urine samples, in a single field-of-views (FoV). We programmed an application to analyse the images and classify detected blobs - potentially ova - using a support vector machine (SVM).

Using the data, feedback and insights gained from testing the stated instrument with schistosomiasis-positive urine samples, the development of a second device that adhered to the standard diagnostic protocols ensued. We present the design choices and the resulting device, which is presently capable of capturing images of the sample over several FoV by manual operation. This system, when fully automated, can assist with the disease control and elimination objectives.

1-2 Thesis structure

The organisation if this thesis document is as follows. Chapter 2 provides information on urinary schistosomiasis, including the life cycle of the parasite, the available diagnostic methods, and a brief study of the standard diagnosis procedure and its drawbacks. The chapter ends with a few mentions, from scientific literature, of attempted methods and possible solutions to simplify diagnosis, and with a summary of our own process. Chapter 3 demonstrates our approach and design choices for the design of two instruments: a mobile-phone microscope and an automated microscope using a Raspberry Pi computer. We also show the images captured using both the devices and an algorithm for ova detection that is deployable on multiple platforms. In Chapter 4, we present the experimental results from the evaluation of the mobile-phone microscope using schistosomiasis-positive urine samples from the field in Nigeria. Finally, in Chapter 5, we mention recommendations for future design approaches, and in Chapter 6 we state the conclusions of this work.

Chapter 2

Background and Thesis Motivation

2-1 Transmission of schistosomiasis infections

Understanding the transmission and effects of any disease is principal to realize a model for its effective diagnosis, control and elimination. In this subsection, we briefly describe the life cycle of the schistosomes. Using this information, in the following subsections, we examine the basis of the modern diagnostic procedures for schistosomiasis.

We now describe the life cycle of the schistosomes. Refer to Figure 2-1 for an illustration to follow along with the text. The cycle begins with the discharge of ova of the relevant schistosome (labelled 1 in the figure) from the definitive host, with urine (*S. haematobium*) or faecal matter (*S. mansoni* or *S. japonicum*). Under suitable conditions, the ovum hatches to release a miracidium, which survives for only seven days [25]. The miracidia swim and penetrate an intermediate host, which in this case is a small tropical freshwater snail. For *S. haematobium*, the primary intermediate hosts are molluscs of the genus *Bulinus* [29]. The miracidia replicate in the snail to form sporocysts which shed free-swimming cercariae, the form that penetrates and infects the definitive host [1, 25, 9], into the water. The cercariae penetrate the skin of the human host and shed their tails to become parasitic organisms called schistosomula. They then move, through venous circulation, to the lungs, followed by the heart and then the liver, where they develop into mature worms. Male and female worms move and reside in specific locations in the mesenteric venules, where they reproduce [11, 1, 25]. For *S. haematobium*, this is in the vesicular and pelvic venous plexus of the bladder. The female worms deposit ova which eventually reach the bladder in the case of *S. haematobium* and the intestine for the other species [1]. The excretion of urine or faeces by the host discharges the ova. When the ova enter water bodies, the cycle starts all over again.

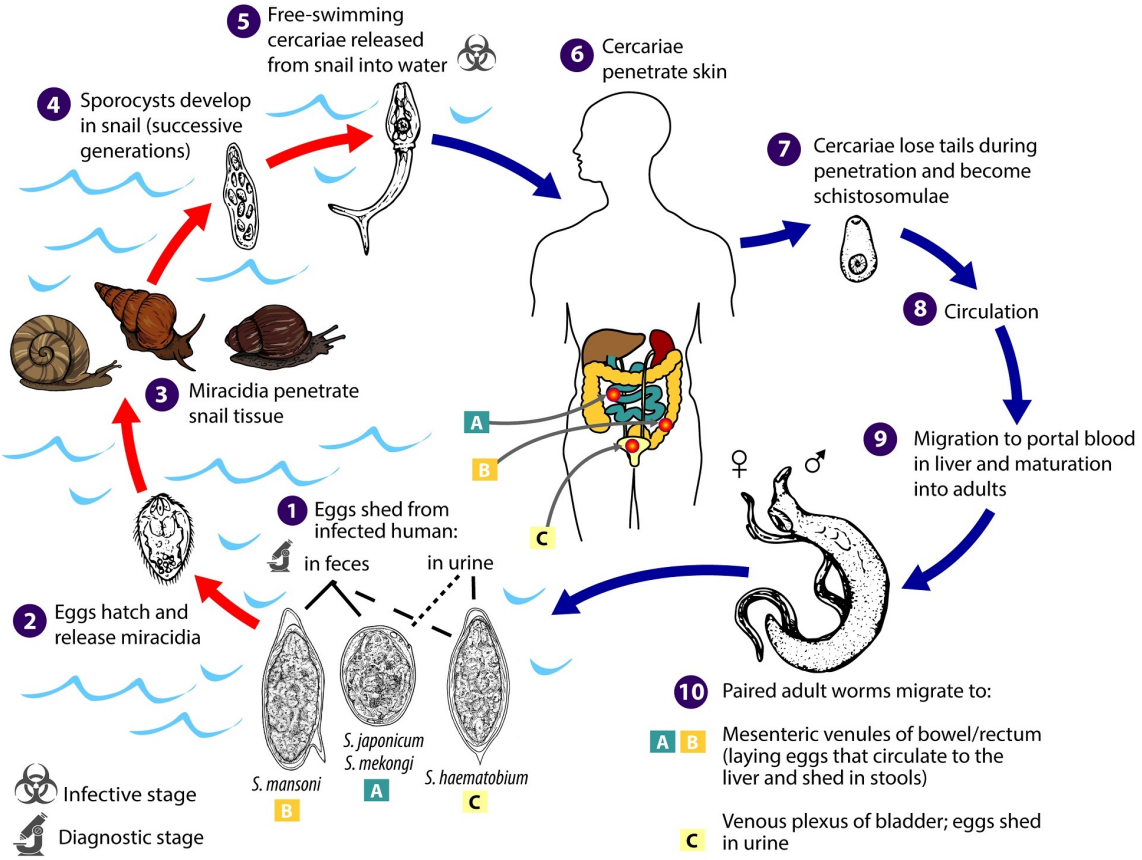

Figure 2-1: An illustration of the biological life cycle of, but not strictly restricted to, the *S. haematobium*, *S. mansoni* and *S. japonicum* schistosomes. Source: Ceneters for Disease Control and Prevention, U.S.A [1]

All statements henceforth are for urinary schistosomiasis. We assume the primary schistosome to be *S. haematobium*. Most of the discussion will also apply to infections caused by the other species. We mention relevant distinctions if and when necessary.

In the next section, we mention many of the available diagnostic tests, their contextual use cases and discuss their performance in terms of the diagnostic sensitivity and specificity.

2-2 Diagnostic tests for urinary schistosomiasis

The choice of a diagnostic test for use in a community depends on the control focus and the diagnostic needs specific to that community [2].

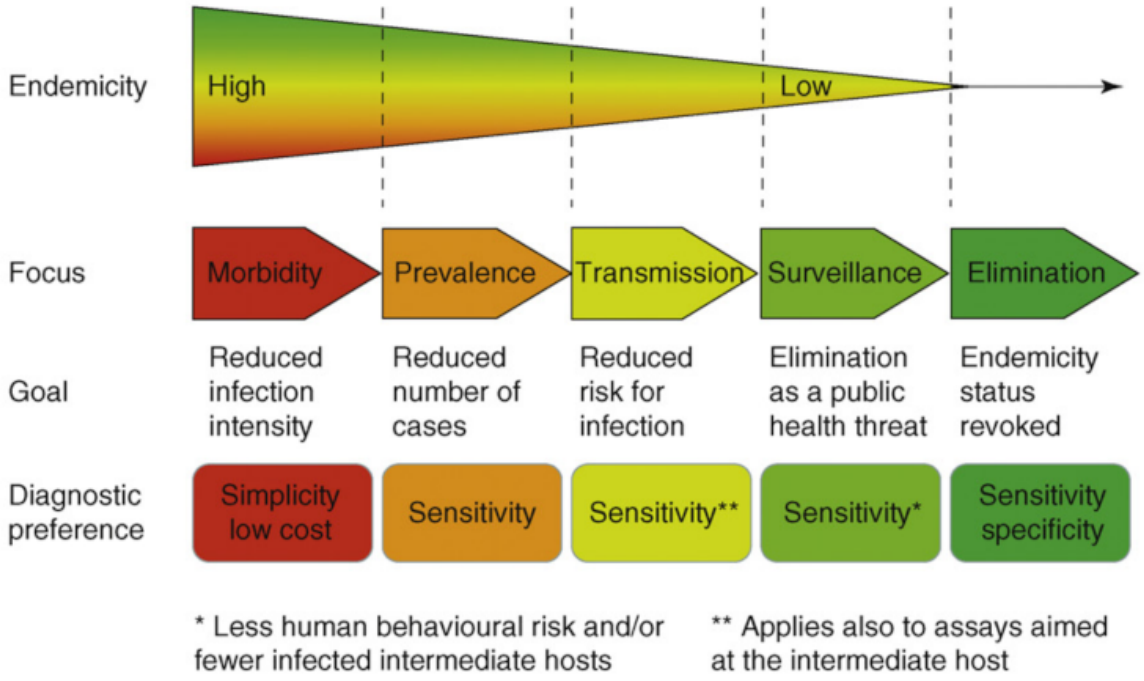

Figure 2-2: An illustration presenting how falling endemicity levels influence control focus and diagnostic needs. Source: *R. Bergquist et al. (2009)* [2]

Figure 2-2 presents the required control focus, goal and the relevant diagnostic preferences for appropriate ranges of decreasing endemicity. The illustration is self-explanatory. For example, for very high endemicity of an infection, the focus is morbidity control - controlling the high incidence of disease in a community - for which highly sensitive diagnostic tests are unnecessary due to higher costs and the complexity of large-scale screening. On the other end of the scale, the point at which the disease/infection is at the verge of elimination, the diagnostic sensitivity and specificity of the tests need to be very high. This requirement is because the prevalence of the disease is so low that it becomes harder to acquire relevant signals (visible parasites, antibodies, etc.) for diagnosis. With this model presented, we now go through some of the available diagnostic tests.

The basis of the available diagnostic tests spans the domains of parasitology, immunology and molecular biology [30]. The standard test for detecting *active* urinary schistosomiasis is to check for the presence of the relevant eggs in the urine. As mentioned in the introduction, examination of filtered urine using direct microscopy is the standard method for the diagnosis, control and mapping of urinary schistosomiasis. However, an important fact to consider is that the larvae need $5-7$ weeks to mature and produce eggs, and during this time, there will be no eggs in the urine [9]. For this reason and because of the limited sensitivity of

urine examination, the search for infecting schistosomes and their effects within the host is essential for *early* diagnosis in endemic zones. Various techniques are under development and evaluation for this approach to diagnosis. Detection of specific DNA fragments in urine and faecal specimens [31], detection of cercarial antigens [21], of relevant antibodies developed in response to the introduction of schistosomal antigens and capturing PET scans for the detection of the adult parasites, are some of the evaluated techniques [16, 22].

The molecular diagnostic tests - like antibody and DNA detection - tend to have a higher reported sensitivity than microscopy and are hence recommended for use in the transmission, surveillance and elimination stages of the control focus [2]. Nevertheless, they do not come without limitations. For example, antibody detection tests cannot quantify the infection load and hence is not applicable in re-examination scenarios. Whereas current DNA tests engender a practical limitation for use in resource-limited settings because they require highly skilled personnel and laboratory space. Due to various factors inclusive of the ones mentioned above, the diagnostic cost per examination for these methods is very high in comparison to the standard method [16].

The standard method, microscopic examination of filtered urine, is available at a fair cost per examination and reportedly furnishes a high diagnostic specificity of $\mathbf{96-100}\%$. However, it lacks good diagnostic sensitivity - over a broad range of $\mathbf{24-100}\%$ - which makes it incompetent for the detection of low-intensity infections. Several techniques exist to increase the sensitivity of this method, like repeated sampling, the collection of larger quantities of urine and pooling of samples, at the expense of increased labour requirement and diagnosis time. Nonetheless, the accessibility, reusability of most equipment and the overall cost-effectiveness of the procedure enabled it to sustain and establish itself as the current reference standard diagnostic method for urinary schistosomiasis [2, 16].

The factors hindering the possibility of raising the diagnostic sensitivity of direct microscopy are avoidable by automating the process of sample observation and egg detection. Such a tool will be precious in the short-term, in resource-limited settings, as it will require minimal operational resources while simultaneously raising the disease diagnosis and surveillance capacity. These features are implementable in a potential portable device, while applying the standard procedural protocols established by WHO and keeping it relatively inexpensive. This thesis work focuses on the development of such a device.

The detection targets for the diagnosis by microscopy are the *S. haematobium* ova. To automate the detection of these biomarkers, we need to study the morphology and features of the eggs, which are also essential determinants in the design of our optical system. In the next section, we present this information.

2-3 Morphology of the ova of *S. haematobium*

The ova of the schistosomes have an elongated oval-shaped structure that is narrower on one end than the other. The primary feature that characterises *S. haematobium* ova is the presence of a terminal spine at the narrow end [32]. This feature is essential for diagnosis because it is what differentiates the urinary schistosomiasis infection from the others if they are present. Co-infection by multiple schistosome species is possible [9].

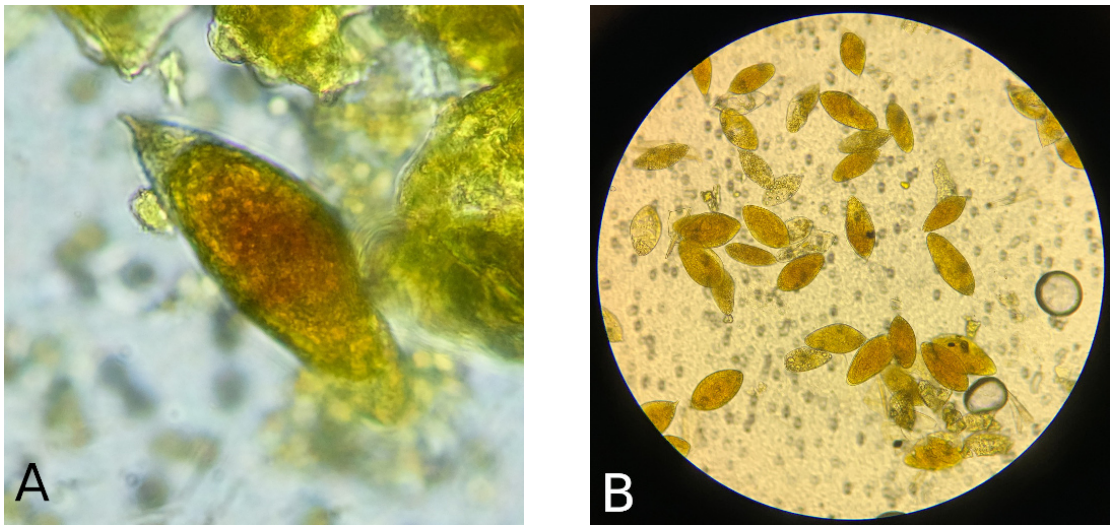

Figure 2-3: (A) An *S. haematobium* ovum (centered in the image) observed using a $\times 40$ objective under a microscope. Note the terminal spine at the top left. (B) ova stained with Lugol iodine visible over a standard filter membrane using a $\times 20$ objective.

The earliest report on the measure of the ovum states about 150 μm $\times$ 60 μm [32]. Statistics show that the ova measure in the range 110-170 μm $\times$ 40-70 μm [1]. Taking note of these dimensions is essential for designing the optical system to resolve sufficiently and acquire images of the ova for the diagnosis and quantification by a computer.

Fresh ova have a thick transparent body, usually showing a translucent miracidium with distinctly noticeable structure. Calcified or dead ova are black with the miracidia structures indistinct [33, 34]. The black ova are apparent in bright-field microscopic images, while the fresh ova are not. To improve the visibility of the transparent ova during observation, a minute amount of Lugol's iodine solution (0.5%) is added to the filtered sample [17]. Counting the number of all, fresh and calcified, ova is essential to precisely quantify the intensity of infection.

2-4 The standard diagnostic procedure

A primary characteristic of the infection is the presence of schistosome ova in the urine excreted by the infected host. The traditional approach to quantifying the intensity of the disease is the number of ova present in 10 ml of urine. The choice of the urine quantity, 10 ml, is due to a meticulous field study conducted in 1976 by *P.A. Peters et al.* [35], which is a recommended read.

This section describes the WHO-approved procedure for diagnosis and quantification that is used today in the field. The required materials, reagents and instruments are listed below, and then the detailed procedure follows. The following procedure is from the WHO manual for a health lab [17] and from the observation of a microscope operator using the standard procedure.

(A) Microscope slides
(B) Coverslips
(C) Filter holder, 13 mm diameter
(D) Membrane filter, $12 - 20$ μm diameter
(E) Plastic syringe, 10 ml
(F) Forceps
(G) Containers for urine collection
(H) Lugol iodine, 0.5% solution
(I) Formaldehyde, 37% solution
(J) 1% hypochlorite solution
(K) Microscope
(L) $\times 4$, $\times 10$ and $\times 40$ objectives

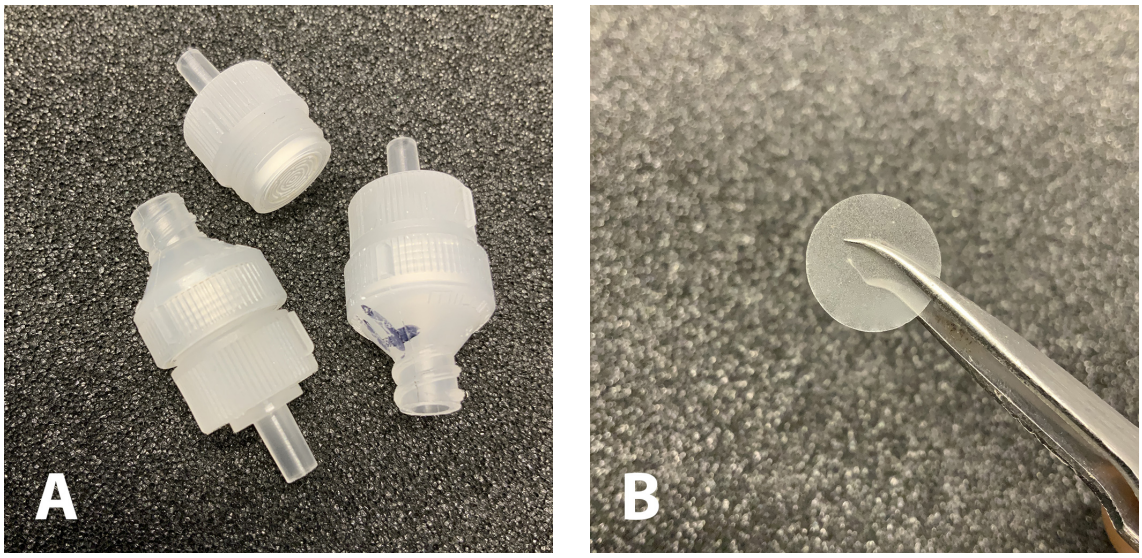

Figure 2-4: (A) Filter holders for a filter of diameter 13 mm, and (B) a polycarbonate track etch (PCTE) membrane filter of diameter 13 mm and pore size 12 μm. The membrane is hydrophilic. We purchased both the materials from *Sterlitech Corporation*, USA.

The filtration procedure

1. Collect at least 10 ml of urine from the patient between 10:00 and 14:00 hours.
2. Preserve the ova if it is not possible to analyse the urine within an hour. For this, add 1 ml of 37% formaldehyde solution to every 100 ml of urine. Else, follow with step 3.
3. Place a membrane filter in the filter holder.
4. Gently agitate the urine sample, draw 10 ml using an unused syringe and attach the syringe to the filter holder.
5. Discharge the urine through the filter over a sink or a bucket.
6. Disconnect the syringe from the filter holder, draw air, reattach the syringe and expel the air through the filter.
7. Disconnect the syringe from the filter holder and open the filter holder. Carefully remove the membrane filter using a forceps and place it face-up on a microscope slide.
8. Add a drop of freshly prepared Lugol iodine solution to the membrane to raise the visibility of the ova that are not calcified.
9. Examine the entire filter over a larger area using a $\times 4$ or $\times 10$ objective under a microscope for the ova. Use a $\times 40$ objective to confirm whether the species is that of *S. haematobium* by looking for the presence of a terminal spine.
10. Record the results as the number of ova present in 10 ml of urine. Qualitative results are recorded as, having a *light* or *heavy* infection for eggs in the range of $1 - 49$ and > 50 respectively.
11. Plastic filters can be reused. Soak the filter overnight in a 1% hypochlorite solution. Wash it thoroughly with a detergent solution, rinse it with clean water and check under the microscope if it is free of parasites.

The procedure is very comprehensive and involves many steps that require careful execution. Steps 3 to 8 in the process are for sample preparation alone. Step 9 and 10 are for the examination and recording the results. The average time for processing a sample, inclusive of sample preparation, as reported in literature, is between $1 - 2$ minutes [35]. However, from our observation of a well trained operator in a lab, the average time is close to 2 minutes and 30 seconds.

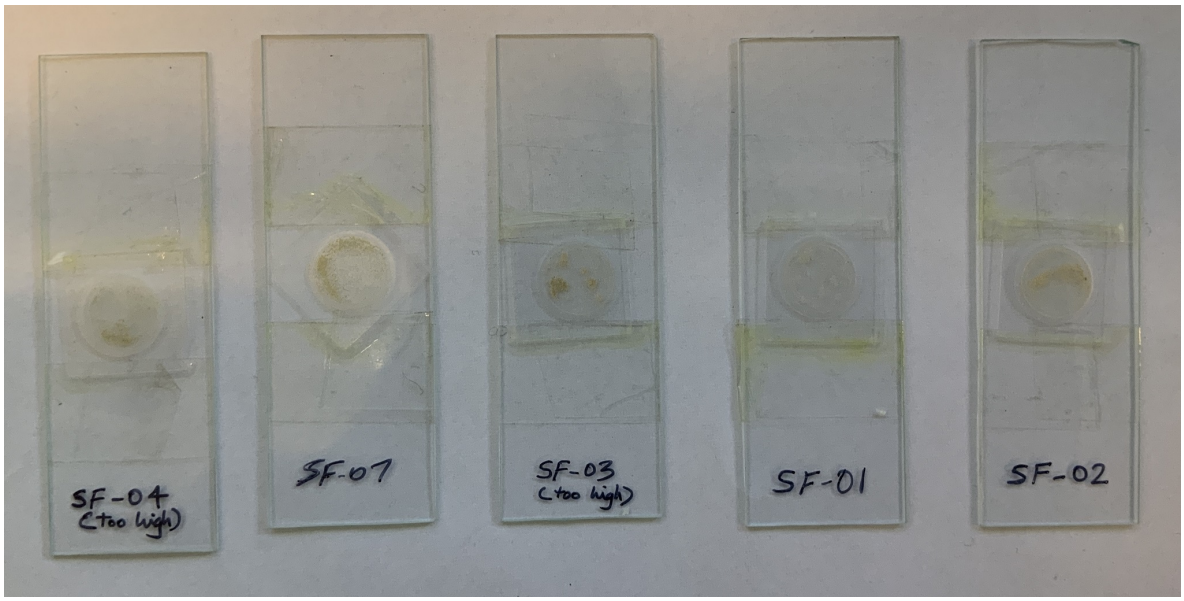

Figure 2-5: Samples prepared for observation.

2-5 The need to automate the standard procedure

There are many reasons, from different perspectives, to automate the diagnosis procedure and potentially embed the technology into a portable device.

From the *available resources* point-of-view, there are countries which lack a sufficient number of trained and experienced microscope operators, and the essential lab equipment, that will need to arrive at the field. Standard microscopes are an expensive initial investment and will require trained personnel to operate and maintain. Moreover, many communities that require mass screening are remote areas that have limited or challenging transportation routes. In this case, the lack of microscope operators implies that urine samples require transportation to a city or town with an adequately equipped laboratory for analysis and the results sent back to the field at a later time.

When considering the *diagnosis performance*, take note that the current sensitivity is modest and is over a wide range [16]. Several of the factors that cause this shortcoming cannot be changed, like the variation in egg count in the urine over the day or week. However, these can be corrected for by techniques like repeated-sampling and collecting more quantity of urine, as mentioned in Section 2-2. Moreover, the sensitivity of the procedure, or any manual microscopy procedure, is not consistent or standardised because the human factor plays a significant role. Preparing and analysing around a hundred samples a day for many days rapidly changes into a dull task. The strenuousness of the procedure can affect the operational performance of even the most competent microscope operator.

2-6 Available solutions in literature

Some of the proposed and tested methods that are available in the literature are listed below.

2-6-1 On-chip imaging of *S. haematobium* eggs in urine

In the work of *Linder E. et al* [3], the authors obtained inexpensive webcams and removed the optical elements. With an appropriate container mounted around the camera sensor, and the proximal electronics protected using silicon or acrylate polymer, they pour infected urine and let it settle on the CMOS sensor chip. For some experiments, they used two different mobile phones and replaced the protective glass of the camera with a coverslip. They then illuminated and imaged the samples.

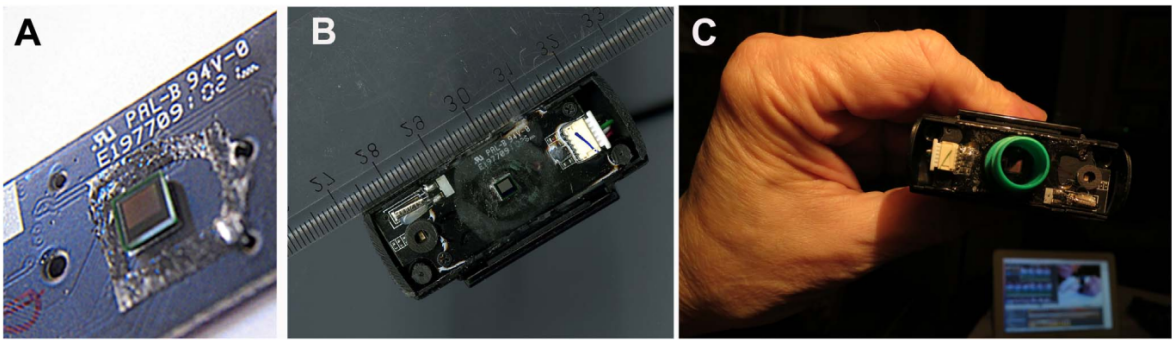

Figure 2-6: (A) The exposed webcam sensor. (B) The proximal electronics protected using a relevant resin, and (C) a tube mounted to form a sedimentation chamber around the sensor. Source: *Linder E. et al* (2013) [3]

The webcam system demonstrated an optical resolution of 12 μm, identified using the *USAF 1951* resolution chart, which is more than sufficient to image the eggs which are $110-170$ μm long and $40-70$ μm wide. The primary advantage of this method is the availability of a large field-of-view of 10 mm^2, which is the sensor area, relative to a conventional microscope or the use of a ball lens. However, the absence of optics can introduce diffraction artefacts in the images, which will require additional reconstruction algorithms for improving image quality. The cameras are models from the year the paper was published, 2013. Modern-day webcams may have larger sensor areas and smaller pixel sizes, but the use of a single camera for a single or a few samples is not economical in the long term. The use of a coverslip to protect the sensor and applying partially coherent in-line holography methods seem promising.

For egg detection, the authors trained a forty-five stage cascade classifier based on Haar-features using 500 cropped images of the eggs with data augmentation. The model demonstrated a diagnostic sensitivity of 71% and a specificity of 79% on a set of seventy-five test image pairs.

2-6-2 Mobile microscopy

Hand-held and mobile-phone microscopy are growing fields [16] and show much promise for the diagnosis of many infections. Positive results from the evaluation of these devices for helminth infections [26], detection of filarial parasites [36] and the detection of tiny parasites for the diagnosis of malaria [27], put these devices in the spotlight.

For standard microscopy, the expensive parts tend to be the optical components. Microscope objectives contain many large lenses to improve image quality by compensating for various optical aberrations that are generally inherent in the system. However, for the identification of relatively large biomarkers, like the ova of *S. haematobium*, we can design small and straightforward optical systems that obtain good images. We factor this in the design of mobile microscopes, which are usually the standalone mobile-phones with an additional inexpensive optical element to modify the system for the observation of small objects.

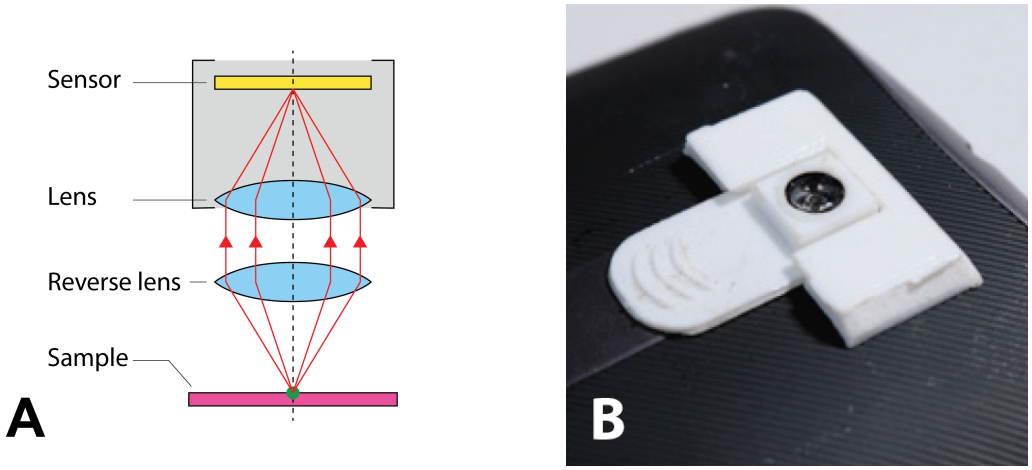

Figure 2-7: (A) An illustration of the reverse-lens setup, and (B) the reverse-lens setup behind our mobile-phone microscope prototype.

One such setup of relevance is the reverse-lens mobile-phone microscope, as demonstrated by *Switz N. et al* [37]. The setup consists of a mobile-phone and a spare lens of the camera of the same phone or another, positioned in reverse. Assume the reverse-lens is similar to that of the phone camera, and we position the sample at the focus of the reverse-lens. This setup supplies a microscope with a magnification (M) of $\times 1$ and a field-of-view equal to the area of the camera sensor. Modern mobile-phone camera lenses have f-numbers (f) in the range of $3.0 - 2.0$, which computes to a numerical aperture (NA) in the range of $0.17 - 0.25$. This range for the NA, which translates to the light-gathering capability of the system, is standard for most available microscope objectives.

Some of the other evaluated mobile-microscopes are a ball-lens based microscope [38, 27], an origami-based paper microscope that costs USD 1.00 called the Foldscope [39], and devices with the microscope objectives mounted to the phones [40, 41]. The Foldscope, reversed-lens Cellscope and the Newton Nm1 microscope with a cellphone attached showed diagnostic sensitivities of 55, 67 and 81%, and specificities of 93, 100 and 97% for *S. haematobium*.

Besides the advantages of the reasonable performance and the low-cost of the optical systems of these devices, they provide several benefits from an operational point-of-view. The devices tend to be very portable and are not affected by the intermittent power service in remote locations. They can perform automated diagnosis using computer vision methods and can upload diagnostic data for aiding burden estimation and disease surveillance [26].

2-6-3 Open-source microscopes

Many open-source microscope designs are available [42, 4, 43, 5]. Their prevalence is due to the presence of convenient manufacturing methods like 3D printing and laser-cutting and the availability of affordable, high-quality components like cameras and optical elements.

We do not evaluate these designs in detail, but we mention some of the advantages and disadvantages. At least one design provides sub-micron stage positioning accuracy [42]. There is a design which costs as little as € 100 which imaged the *S. haematobium* ova [4] to an adequate level of resolution. Similar to the open-source philosophy of the manufacturing designs, the hardware and software also use accessible open-source technologies. A Raspberry Pi computer [44] along with a standard Raspberry Pi camera [7] augmented with additional optical elements is in use with today's open-source projects.

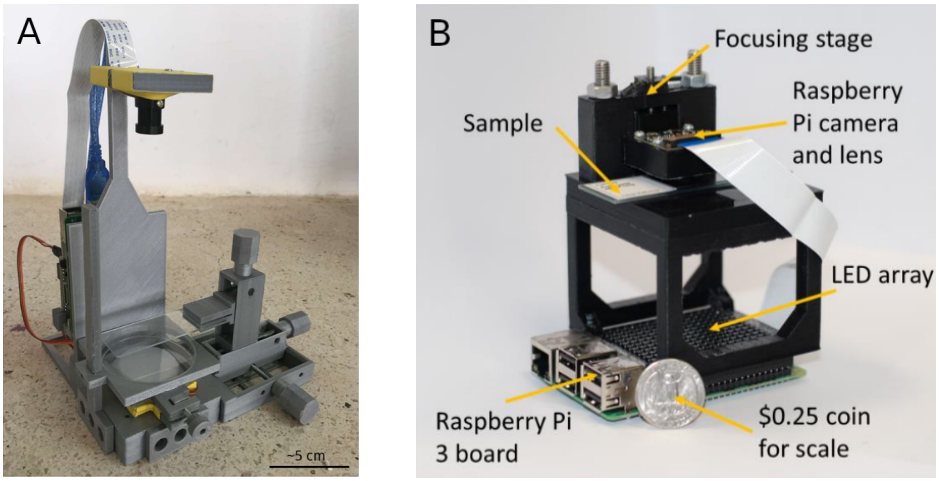

Figure 2-8: (A) The €100 *Lab* microscope built using 3D-printed parts and relevant electronics (2017) [4]. (B) A low-cost Fourier Ptychographic microscope that costs USD 150 (2018) [5]. Both the devices use a Raspberry Pi as their computer.

A standalone microscope will still need an operator to control it, which limits their use in a labour-limited setting. This drawback is avoidable by automating the imaging and detection stages. However, automating the microscope stage requires the use of reliable stepper motors with precise positioning, which are usually expensive and bring the total cost of the system to that of a standard microscope or beyond.

2-7 A summary of our approach

Using all the information presented up to this point, the potential design directions and consequently the objective of this thesis work are outlined below.

Molecular methods seem to be the most straightforward diagnostics in terms of the ease of use and speed of diagnosis. These methods, however, can be deployed on a large scale only after significantly reducing the cost per diagnosis and simplifying the use of the devices. Until then, standard microscopy will hold steady for the diagnosis of urinary schistosomiasis. Operating the microscopes will be difficult in scenarios with limited access to experts, and hence device automation is necessary. So, we work towards designing an automated microscope that is also very cost-effective, specifically for diagnosing urinary schistosomiasis.

Sample preparation is still required and is a hectic task, but it is a skill that is quickly learnable by relevant members of local healthcare centres. It may be possible to automate this process as well, but we do not focus on this aspect as it will require a different research direction. Methods of diagnosis without the need for sample preparation, like the research work presented in Section 2-6-1 [3], are a potential solution. Lensless imaging methods, like in-line holography, seem to show promising performance. Lensless imaging methods are currently under active research and development at the smart optics for diagnostics group at the faculty of Mechanical, Maritime and Materials Engineering (3mE), TU Delft.

We approach the design of structural components and the embodiment with a focus on reproducibility by relevant potential local producers in the endemic countries like, for example, makerspaces. Local production will assure local availability as well as local support for maintenance and repair. The two main focus areas for distributed production are 3D printing and laser-cutting machines since they are currently widely available in Africa, for example in Nairobi, Kenya and Lagos, Nigeria. At the faculty of Industrial Design Engineering (IDE), TU Delft, there is ongoing field-research in sub-Saharan Africa to identify the specific needs and device features for automated diagnostic devices. This research is in collaboration with local makerspaces in Nigeria and Kenya.

Concerning the device technology, to automate the stage, we use inexpensive stepper motors with sliders and propose an approach using scene-recognition to increase their operating reliability. For the optical system, we use the Raspberry Pi camera augmented with a reverse-lens. This configuration will provide a magnification of $\times 1$. Conventional microscope designs enable the use of objective lenses that provide higher magnifications ($\times 4$, $\times 10$, $\times 20$ and more). However, such systems will tend to be larger because they require a mechanical tube length in the range of $160 - 200$ mm. Whereas using the reverse-lens configuration, the ideal tube length is null, and hence we can maintain a compact system design. We show that the magnification of $\times 1$ is adequate to image the *S. haematobium* ova while using the Raspberry Pi camera.

Chapter 3

Method

In this chapter, we describe the development of the mentioned device. The description contains three sections: the choices and development of the hardware (Section 3-1), the acquired images (Section 3-2) and our ova detection method (Section 3-3).

Before the development of the automated microscope, we designed, prototyped and evaluated a mobile-phone-based reverse-lens microscope. For this reason, the experimental procedure and evaluation will also contain details regarding this device. The development of the automated microscope ensued because of specific issues faced when evaluating the mobile-phone microscope, which are elaborated in Section 4-1.

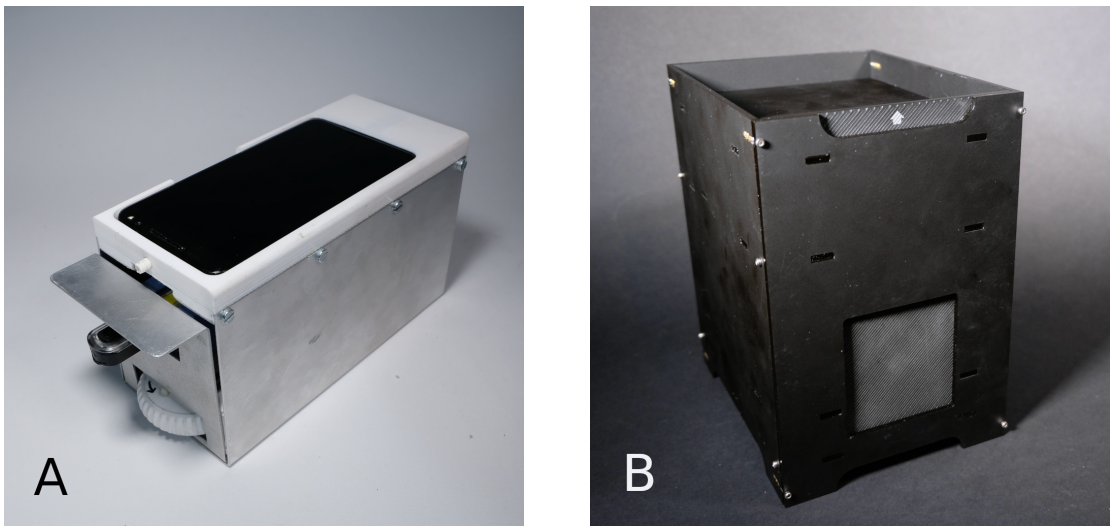

Figure 3-1: (A) Our mobile-phone-based reverse-lens microscope design, and (B) our current iteration of the low-cost reverse-lens automated microscope.

3-1 Hardware

The hardware constitutes all the fundamental elements required to at least manually control and image the target sample for analysis. We discuss the choice of the optical and imaging hardware for the instrument, the computer to control the device, the utilised mechanical components for moving the camera/sample and focusing the urine sample, and the design of the embodiment.

In the last section (3-1-5), we proposed a basic model for a component needed to re-calibrate the device. This model can potentially replace the calibration switches that are generally a part of automated microscopes, thereby minimising the use of mechanical components and hence lowering the chances of mechanical fault.

3-1-1 The optical hardware

Mobile-phone-based microscope

For the evaluated mobile-phone microscope, we used the Moto X Style 2015 smartphone. The relevant technical specifications of the phone camera are listed below.

Feature	**Value**
Price of device	US$ 150
Sensor resolution	5344×4016 pixels
Sensor image area	5.985×4.497 mm
Pixel size	1.12 μm
Spatial resolution (theoretical)	2.24 μm
Focal length	4.6 mm
f-number	2.0

Table 3-1: Relevant technical specifications of the camera module (SONY IMX230) on the Moto X Style 2015 smartphone.

The experimental setup consists of the mobile-phone augmented with a spare lens as the reverse-lens over the rear camera. We built a sheet-metal housing around the device to house a sample holder with the diffuser. The intended goal of this device is to analyse and diagnose urinary schistosomiasis in a single FoV, rather than over multiple FoVs using the standard filter. The optical apparatus of this device cannot image the entire standard filter without moving the sample along the X and Y axes. We use cloth with a pore size of $18 - 36\mu$m to filter the urine.

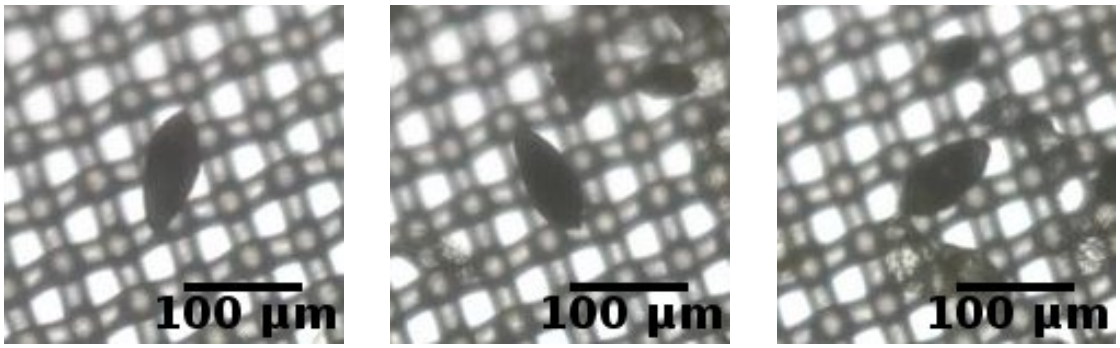

Figure 3-2: Images of the cultured ova captured using the mobile-phone microscope.

The computer for this device is the mobile-phone itself. Refer to Figure 3-1A for a quick view of the entire device.

Automated microscope using a Raspberry Pi

With the open-source philosophy in mind, we utilise an easily accessible and community-supported camera module for the automated microscope - the Raspberry Pi Camera V2. Some relevant technical specifications of the camera are listed below.

Feature	**Value**
Price	US$ 25
Sensor resolution	3280×2464 pixels
Sensor image area	3.68×2.76 mm
Pixel size	1.12 μm
Spatial resolution (theoretical)	2.24 μm
Focal length	3.04 mm
f-number	2.0

Table 3-2: Technical specifications of the Raspberry Pi V2 camera (SONY IMX219) module [7].

From the Nyquist-Shannon sampling theorem, the theoretical spatial resolution for the imaging system is twice the pixel size (1.12 μm). Hence, this value for the camera is 2.24 μm. Taking note again, the size of the ova are within the bounds $110 - 170 \times 40 - 70$ μm, which makes the sensor more than sufficient to image them. However, the spatial resolution can also be affected by the optical components in the system. In practice, we calculate the spatial resolution by the ability of the system to distinguish closely spaced lines in an image. One of the most commonly used target for this is the *1951 USAF Resolution Test Chart*. We image this test chart using our device, after augmenting the reverse-lens and mounting the camera, to ensure that it is stable before sensing any images. Refer to Figure 3-10 for the result.

For the proof-of-concept, we obtain the reverse-lens by removing the lens of a spare Raspberry Pi camera. A prime necessity for the reverse-lens microscope construction is to minimise the distance between the lenses as much as possible - ideally null. Not doing so will result in images with decreasing intensity as one moves away from the axis.

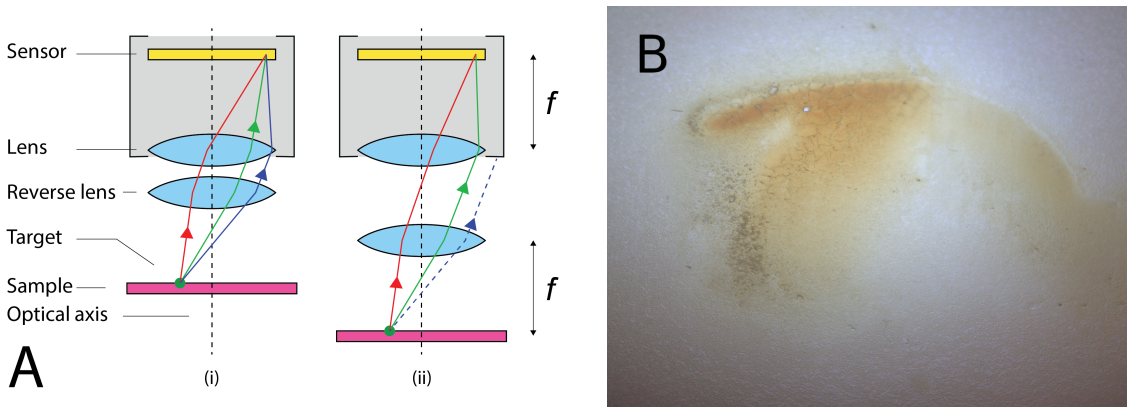

Figure 3-3: (A) The same rays emerging for an off-axis target with (i) the lenses placed as close as possible and (ii) the lenses separated by a longer distance. The cone of light incident on the first lens is the same in both cases. The ray that is coloured blue does not contribute to image formation in the second case. (B) An image of a blood smear captured using our device with the lenses separated by a small distance (~ 3 mm). Note the intensity drop away from the centre.

To mount the reverse-lens on the Raspberry Pi Camera, we tested three different iterations using 3D printing and laser-cutting before settling with a 3D printed design with the possibility of quickly accessing the lens for maintenance. Refer to the figure below for a quick view of the three iterations. More images are available at the end of this subsection.

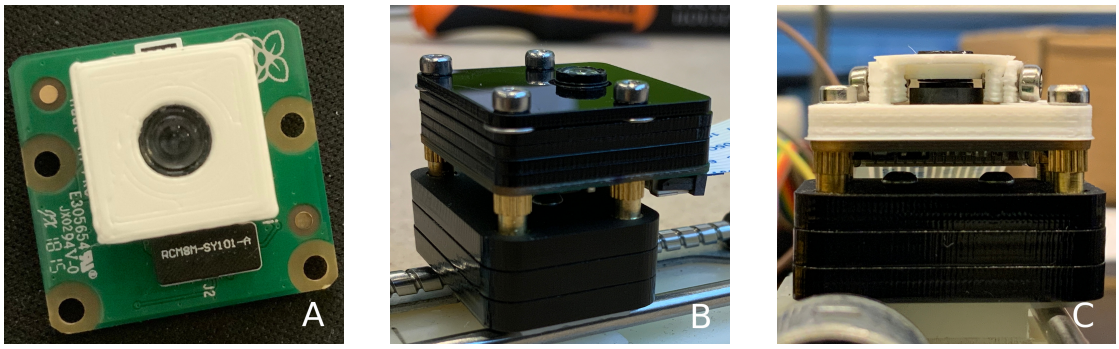

Figure 3-4: (A) The first iteration of the reverse-lens mount which tightly fits around the camera module. Accessing the reverse-lens is harder, since the cap is a tight fit. (B) A laser-cut design using acrylic sheet. The reverse-lens can be removed by disassembling the unit, but the procedure is cumbersome. (C) The final iteration, using 3D printing, that we settled with for this work. The reverse-lens is mounted with a plastic cap that can be screwed to the camera mount.

The selected camera imposes a problem. The sensor plane is not parallel to the surface of the circuit board, because the on-board camera (SONY IMX219) comes attached to the board using a double-sided sticker, which results in a tilt. We can compensate for the tilt by

tilting the reverse-lens in the opposite direction, using an appropriately designed mount, but this design will not translate with all the camera modules since the sticker placement is not predictable. Tightly mounting the revers-lens with the designed plastic cap reduces the tilt to an extent. We propose focusing the sample in different areas of the field-of-view, which will make the system more robust from the software end. Future research focus can include finding the optimal camera and integrating it along with the focusing software for improved reliability.

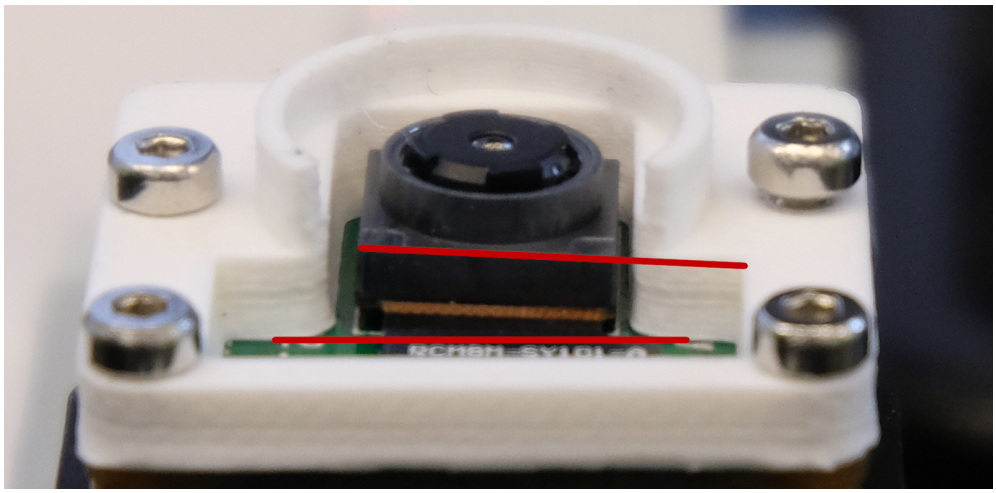

Figure 3-5: The tilt of the Raspberry Pi camera module relative to its circuit board. The bottom red line drawn on the surface of the circuit board and the upper red line drawn on the camera illustrate the tilt.

We now discuss the sample illumination procedure. Refer to Figure 3-6 for the illustration. The inverted cone, with half-angle α representing the aperture, represents the limit of light that can enter the objective.

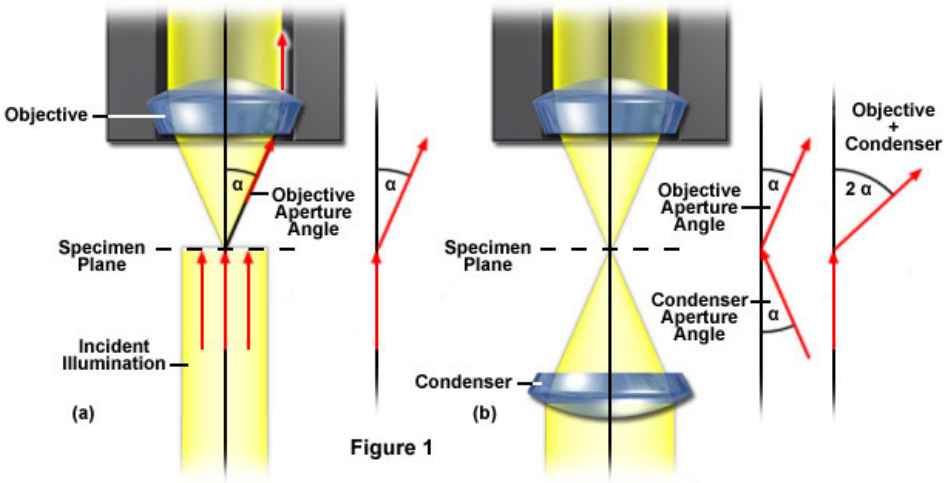

Figure 3-6: Numerical Aperture for microscope objectives and condensers [6]

In a conventional microscope without a condenser, a collimated beam is incident on the sample under observation (Figure 3-6a). Increasing the effective aperture translates to an increase in the resolving power of the microscope. To achieve this, a condenser is added (Figure 3-6b), which generates a ray cone on the illumination side of the specimen. This setup allows the objective to collect light that is a result of larger diffraction angles, which increases the resolution of the system. We achieve maximum resolution when the objective aperture angle matches the condenser aperture angle [6].

In our system, we use an opaque white acrylic sheet of 3 mm thickness that is simultaneously a diffuser and the sample holder. We use this setup to limit the use of expensive components and to maintain a low physical profile. However, the illumination setup may require some tuning to improve the resolution of the optical system. The entire sample platform - the diffuser and sample holder - remains stationary along the X and Y axes, and the focusing mechanism is the same as that of a conventional microscope, where the sample can move along the Z-axis.

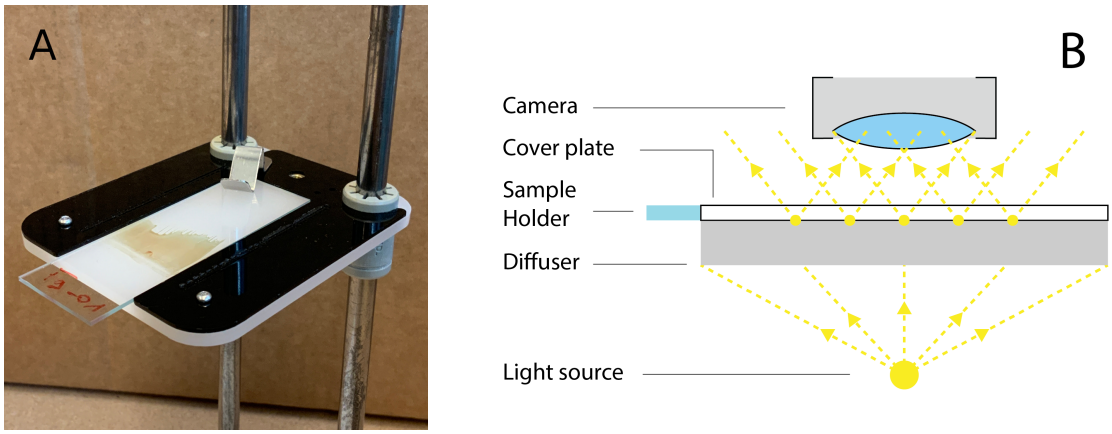

Figure 3-7: (A) The sample holder and the acrylic diffuser with a glass slide of thin blood smear mounted. (B) The sectional view of the diffuser and sample holder setup. We state the purpose of the cover plate - black material in (A) and illustrated in (B) - in Section 3-1-5.

The figure below shows regions with ova captured using the described experimental setup.

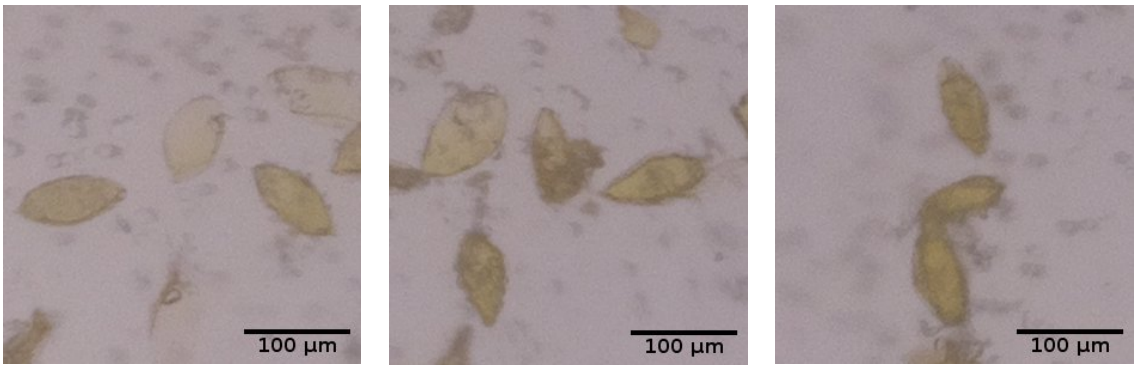

Figure 3-8: Sample images of the ova, from samples cultured at LUMC, Leiden, captured using our experimental setup.

The final setup has the camera mounted on top of an XY-stage consisting of two inexpensive stepper-motors. One motor is fixed and it translates a second motor which moves the camera. We discuss the technical specifications of the motors in Section 3-1-3.

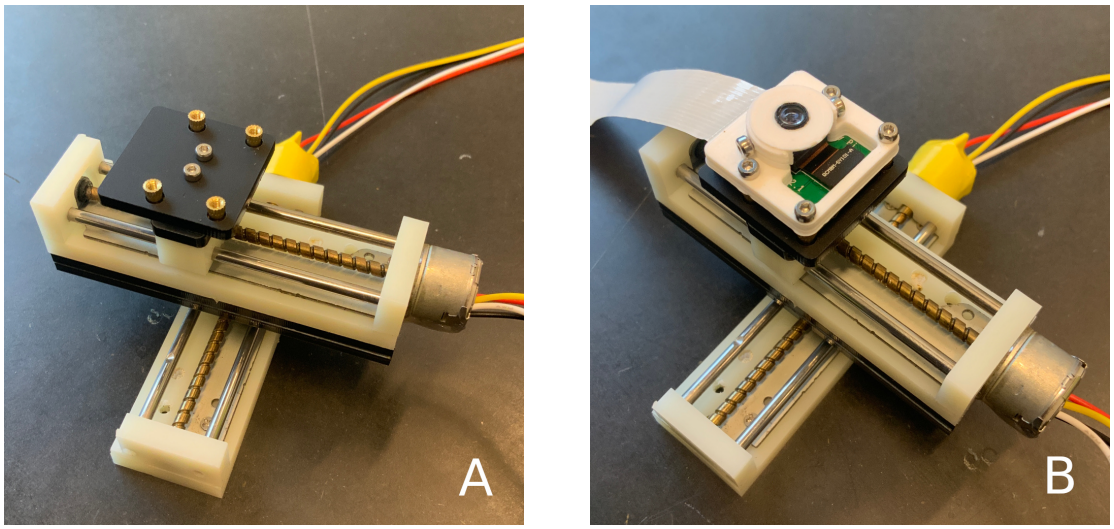

Figure 3-9: (A) The mount for the camera with the XY motors. (B) The camera mounted on top of the XY stage.

The description of the optical setup is complete. Figure 3-10 shows the result of imaging the USAF 1951 resolution test chart. The device resolves line pairs of element 1 in group 8. This result corresponds to 256 line pairs per mm or a line of width 1.95 μm.

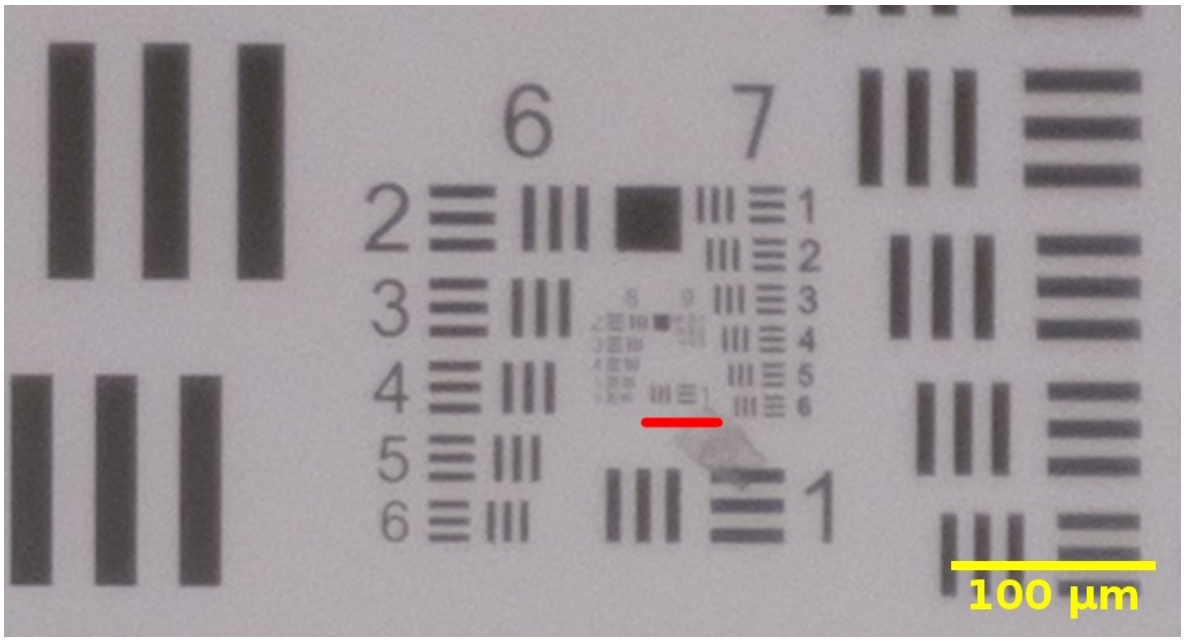

Figure 3-10: The system resolves group 8 element 1 (G8E1).

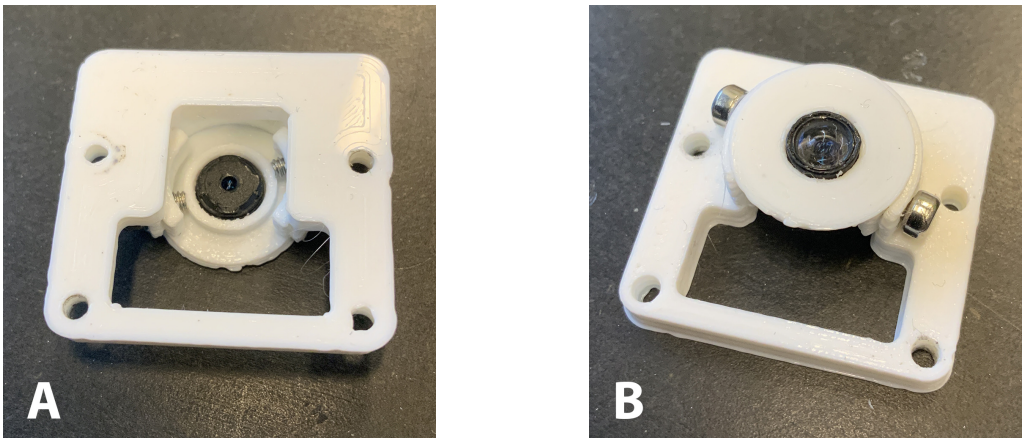

Figure 3-11: (A) Bottom and (B) top views of the Raspberry Pi camera reverse-lens mount.

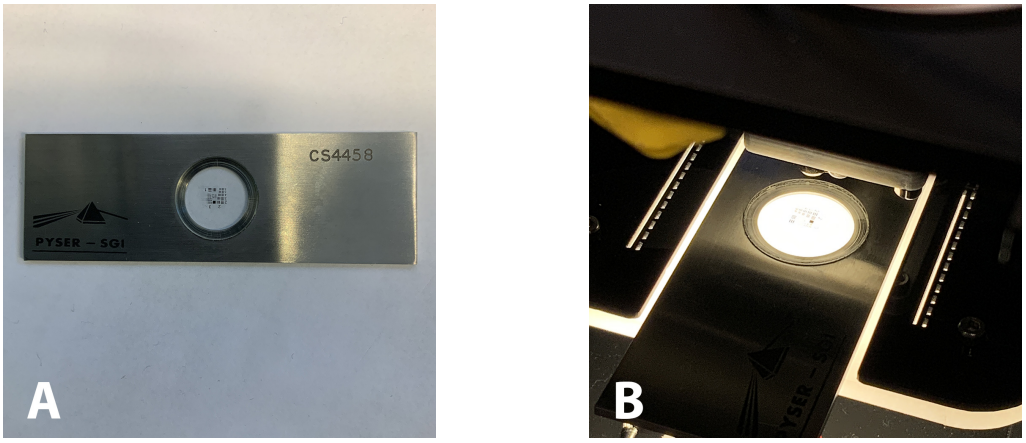

Figure 3-12: (A) The utilised USAF resolution test slide, and (B) the resolution test slide placed on top of the sample holder in our device.

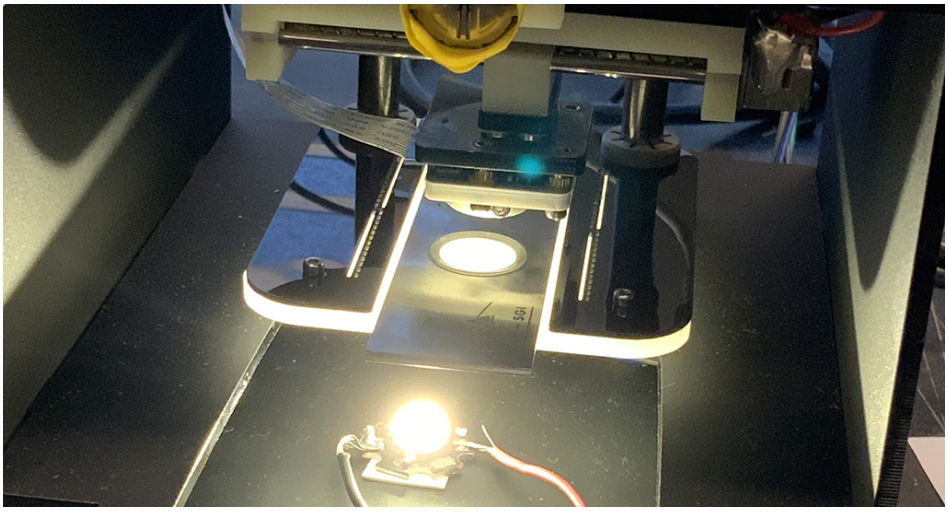

Figure 3-13: The experimental setup with the USAF resolution test slide mounted.

3-1-2 The Raspberry Pi computer

The Raspberry Pi is a low-cost, credit-card sized computer that runs a variant Linux distro called Raspbian, which is in use by many communities ranging from individual and group hobbyists to academic researchers. The computer abstracts away many of the low-level implementation details by providing an accessible high-level interface for the prototyping and testing of embedded systems.

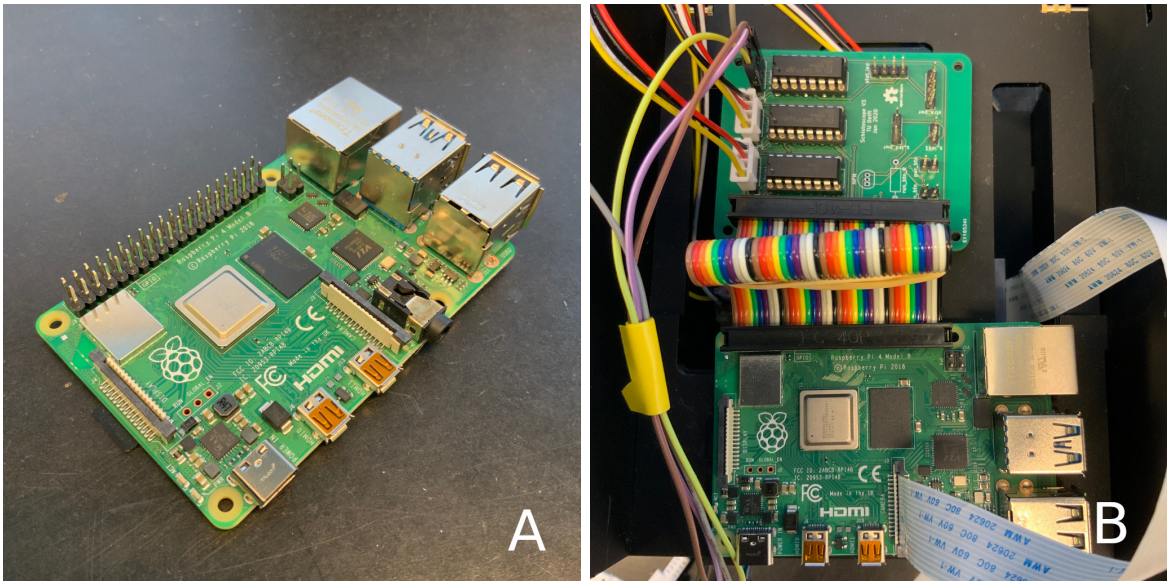

Figure 3-14: (A) The Raspberry Pi 4 computer used in our device. (B) The computer connected to a custom printed circuit board (PCB) and the camera cable (in white with blue text).

The computer provides a high-bandwidth interface to connect and use various camera modules, including the Raspberry Pi camera, and sufficient general-purpose input-output (GPIO) pins to communicate with sensors and drive electronic components. The current high-end version of the computer, the Raspberry Pi 4B (4 GB), is adequate to image targets and drive the XYZ motors, as already demonstrated using the older Raspberry Pi versions by the open-source microscope projects cited in Section 2-6-3. This fact implies that the device is assured to work at least to the level of automatically scanning the target sample, with the use of appropriate auto-focus software.

The final aspect that we need to address is whether the computing power is sufficient to detect ova in the images sensed by the device. We show that it is possible to run image processing and simple image classifiers using pattern recognition models for ovum detection. What remains is to evaluate whether state-of-the-art computer vision models, especially image classification and object detection models based on deep learning, are deployable on this computer. Many online communities (hobbyists and organisations) benchmarked deep learning model inference on the Raspberry Pi 4, showing that there exists at least one model that can serve our purpose [45, 46].

3-1-3 Mechanical components

For the proof-of-concept, the essential mechanical components are only the three low-cost stepper-motors, two of which move the camera along the XY-axes and the other drives the sample stage along the Z-axis for focusing. Both categories of motors are two-phase four-wire stepper-motors.

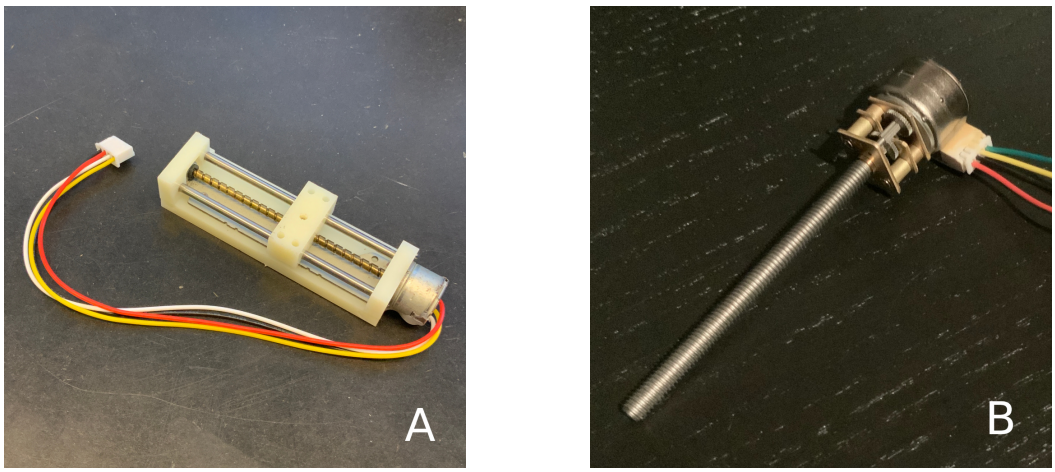

Figure 3-15: (A) An XY-axis motor which comes with a slider and two support shafts, and (B) The Z-axis stepper-motor with an M4 thread shaft.

We drive each of the three motors using an L293D integrated circuit (IC), which are high-current quadruple half-H bridge circuits. The technical specifications for the motors are listed below.

Parameter	**XY motor**	**Z motor**
Product ID	N/A	GA12BY15-M455
Price	€10	€10
Type	2-phase 4-wire	2-phase 4-wire
Drive voltage	$4 - 6$V	5V
Max current	500 mA	300 mA/phase
Shaft	3 mm pitch	M4 screw thread
Effective stroke	57.6 mm	55 mm
Step angle (θ)	18 deg	18 deg
Gear ratio (g_r)	1 : 1	1 : 100
Linear actuation (full-step)	150 μm	0.35 μm

Table 3-3: Some relevant specifications of the motors.

The step angle for both motors is 18 degrees/step. Both the shaft threads are single-start with a pitch (p) of 3 mm and 0.7 mm (M4 thread pitch) for the XY and Z motors respectively. Using these specifications, the linear actuation distance per step (d), for these motors, is computable using Equation 3-1

$$d = \frac{p \text{ (in mm)}}{\frac{\text{Total angle per revolution}}{\theta}} \times g_r \quad \text{mm/step} \quad = \quad \frac{p}{\frac{360}{18}} \times g_r \quad \text{mm/step} \tag{3-1}$$

The actuation distances per step for the XY and the Z motors are 150 μm and 0.35 μm respectively. The linear actuation distance and the effective stroke (refer to Table 3-3) are more than sufficient to move across in small steps over the standard filter (diameter 13 mm) and to focus the ova.

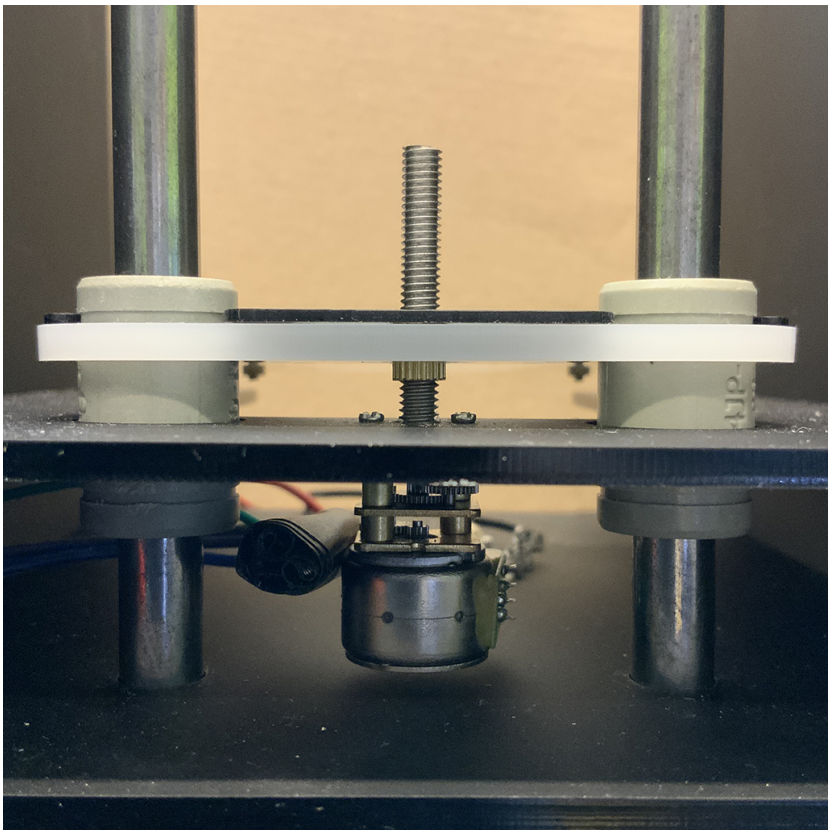

Figure 3-16: The sample holder mounted to the Z-motor shaft using an M4 threaded insert.

3-1-4 The embodiment

The final and optimal design of the embodiment is of limited relevance to this thesis work and should be the focus of experienced design engineers. We explored two models for this proof-of-concept: one using 3D printing and the other with laser-cutting. We started using 3D printing but switched to laser-cutting because of the long printing time for changing design iterations. For demonstrating the device, the laser-cutting approach allowed for quick and iterative prototyping.

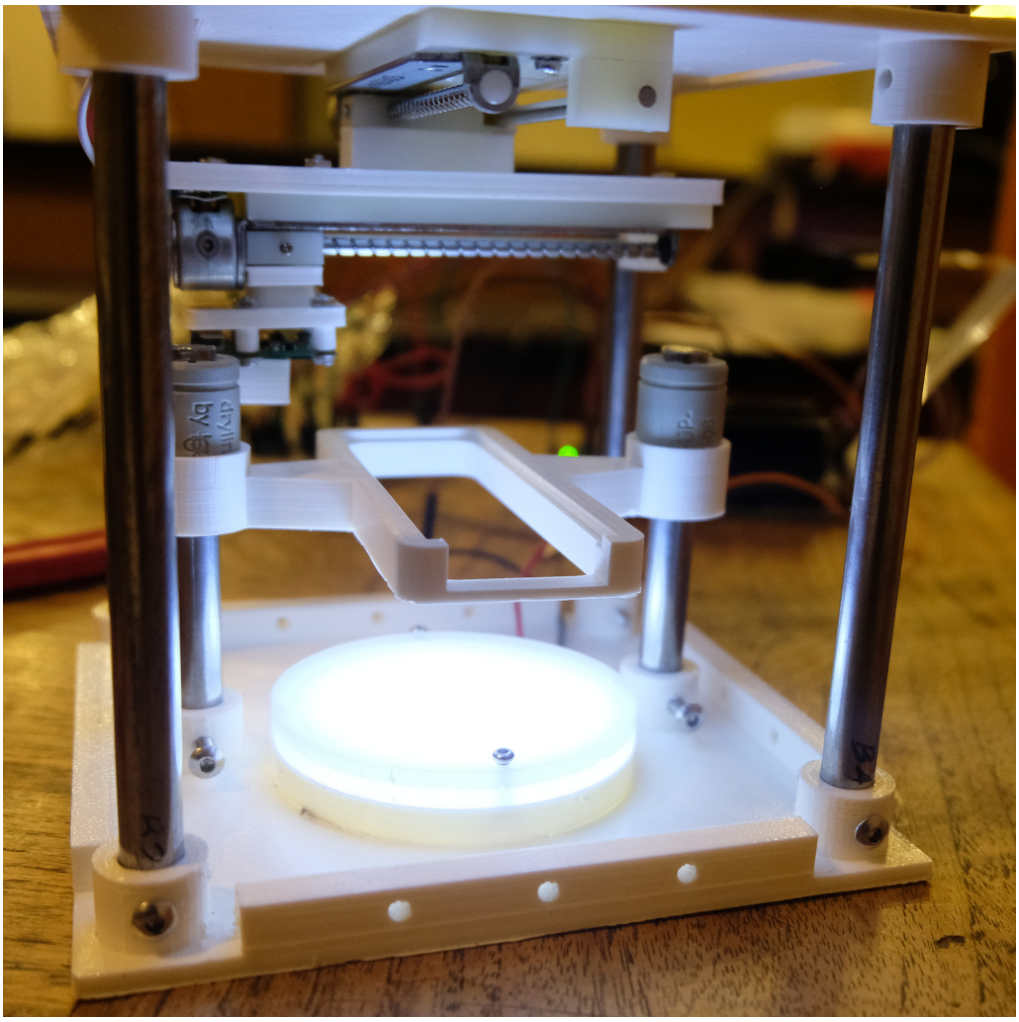

Figure 3-17: Our first 3D printed embodiment design (with outdated interior components).

3D printed components are durable and provide better structural support than laser-cut acrylic sheets, but it takes too long to print them. This downside made it a poor choice for quick iteration. All the plastic components that are part of our outdated design in Figure 3-17 took around 40 hours in total to print, while the laser-cut model in Figure 3-18 took about 6 minutes to cut and $5 - 10$ minutes to assemble.

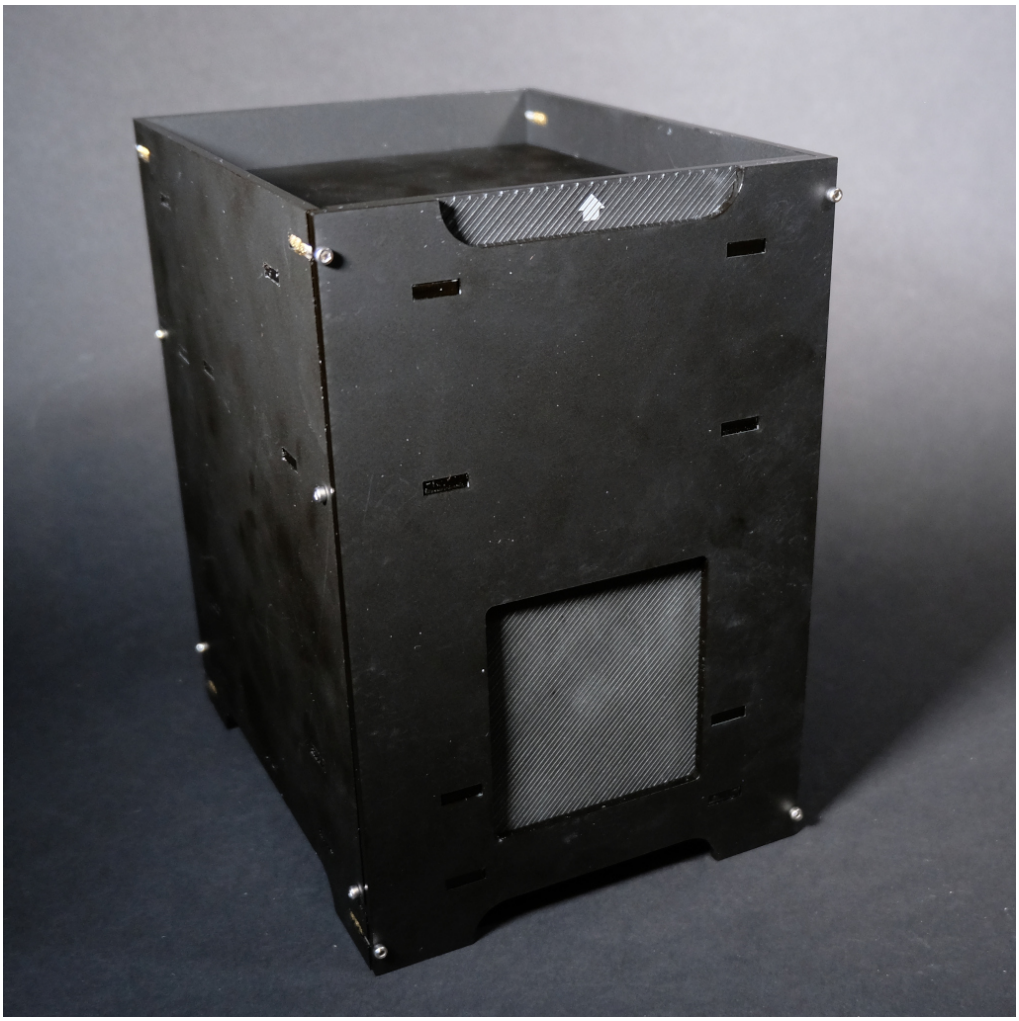

Figure 3-18: Our laser-cut embodiment design.

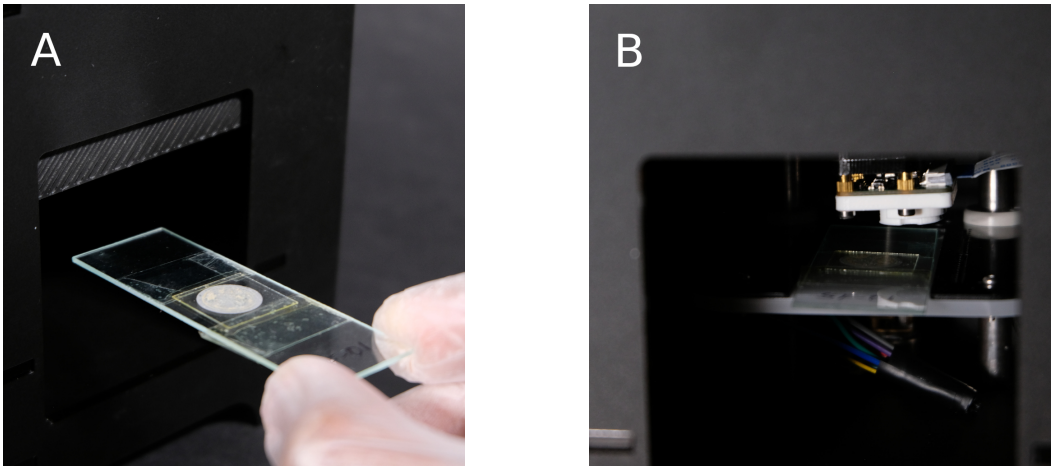

Figure 3-19: (A) A slot to insert and place the sample over the sample holder. (B) The sample placed on the holder with the reverse-lens camera positioned on top.

3-1-5 An alternative to calibration switches

Automated instruments like 3D printers, microscopes and camera stages require accurately positioned switches to re-calibrate or signal to home after every task. This design is necessary because the stepper-motors operate in open-loop and the computer is unaware of any slipping that occurs during operation. Generally, engineers integrate highly-reliable stepper motors which eliminate the problem to a significant extent. Since we use low-cost stepper motors that are not as reliable, these switches are an absolute requirement. We drop the use of switches, to minimise the use of mechanical components, and use the image data for calibration. We propose the design of a cover-plate with slots in a specific pattern. Detecting these slots using the microscope camera enables defining a start- and end-position for the scanning procedure.

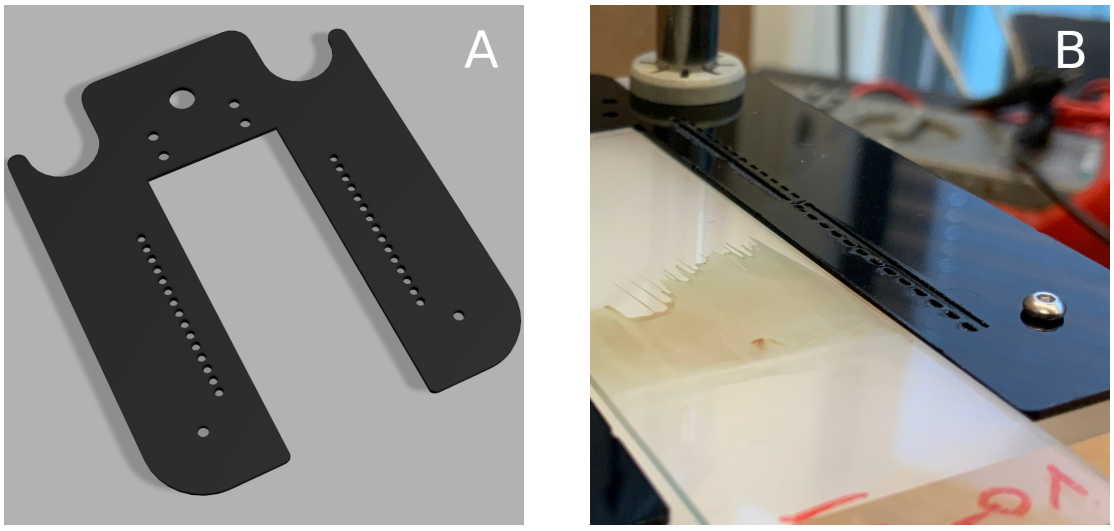

Figure 3-20: (A) A computer designed model of the cover-plate for the sample holder with holes on the sides. (B) A laser-cut cover plate (in black) of 1 mm thickness on top of the diffuser.

The thickness of the cover-plate is 1 mm, which is the same as the glass slide on which the filtered sample rests. The idea is to use recognisable markers to move the camera back to a reference point after every scan. In the case of the 3D model shown in Figure 3-20A, the camera moves to one side and records the arrival at home along the X-axis when circles are in the FoV. The camera then moves up until no more holes enter the FoV, and records home along the Y-axis. Next, we lower the sample stage by a few millimetres to ease sample removal and insertion. After the insertion of a new sample, the scanning process begins by first focusing on the holes. This step assures that the camera is focusing on a proximal plane to the urine filtrate since the cover plate with the markers is as thick as the glass slide. The camera then moves left and down attempting to find the curvature of the filter and then scans the entire filter as a grid of images (multiple FoVs), and this process repeats for the next sample.

This procedure can potentially help in running the whole system in closed-loop by keeping track of the area explored by the camera for each filtered sample. Determining stepper-motor slipping will require comparing the previously captured image with the latest one after sending the command to step along the X or Y axis.

The design of the cover-plate requires more consideration — specifically, the choice of the pattern for detection. In Figure 3-20, we show two examples: one with holes and the other with slots. Both of them are laser-cut acrylic sheets. Truly, we may only need a thin and long slit.

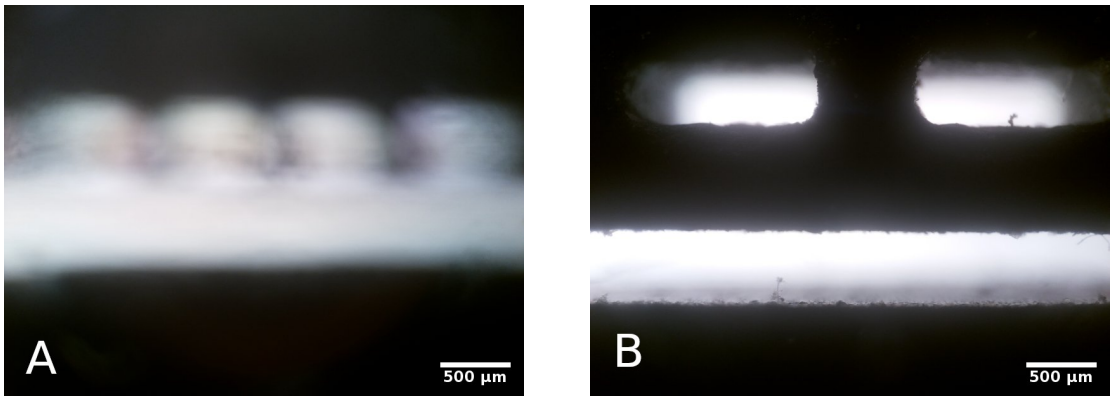

Figure 3-21: The above images are for the cover-plate shown in Figure 3-20. (A) The out-of-focus image of the slots. (B) The image with the slots in the focal plane of the optical system.

One minor concern we ran into when testing this method is, on moving the sample closer to the camera after focusing, the inner-layers of the acrylic sheet start to come into focus. Refer to Figure 3-22 for images of this result.

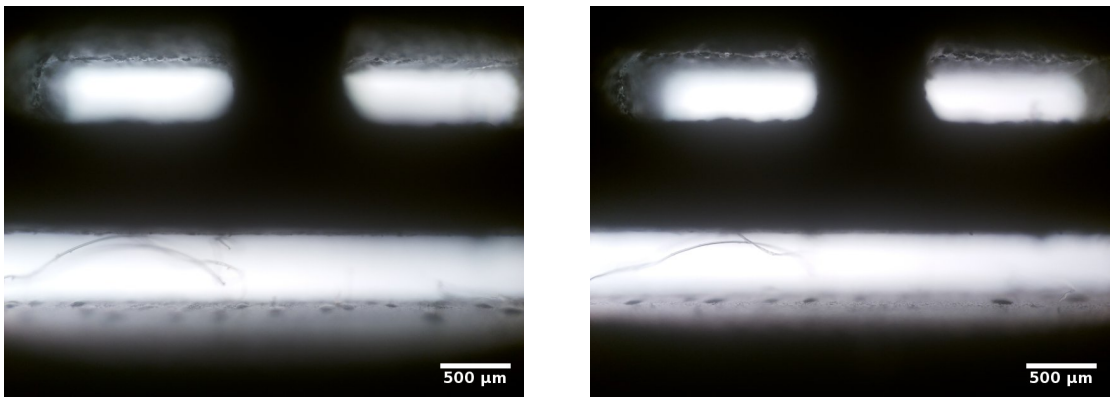

Figure 3-22: The inner-layers of the acrylic sheet in focus.

The above result does not pose any issues for the automation of the device. Robust detection software can overcome this event. However, to minimise the software complexity that deploys on the Raspberry Pi, it is wise to optimise the model on the physical device to a considerable extent. One possible approach to overcome this concern is to make the slots taper outward in the direction of the inner layers. This method will require 3D printing instead of laser-cutting. For example, instead of circular holes resulting in the removal of cylindrical volumes, the cover-plate will have frustum cavities.

3-2 Acquired images

3-2-1 Using the mobile-phone microscope

For the microscope using the mobile-phone, a single image constitutes the entire sample. With the setup described in Section 3-1-1, we captured the images, with dimensions 4016×5344 pixels, shown in Figure 3-23. The cropped regions in Figure 3-24 are 2048×2048 pixels.

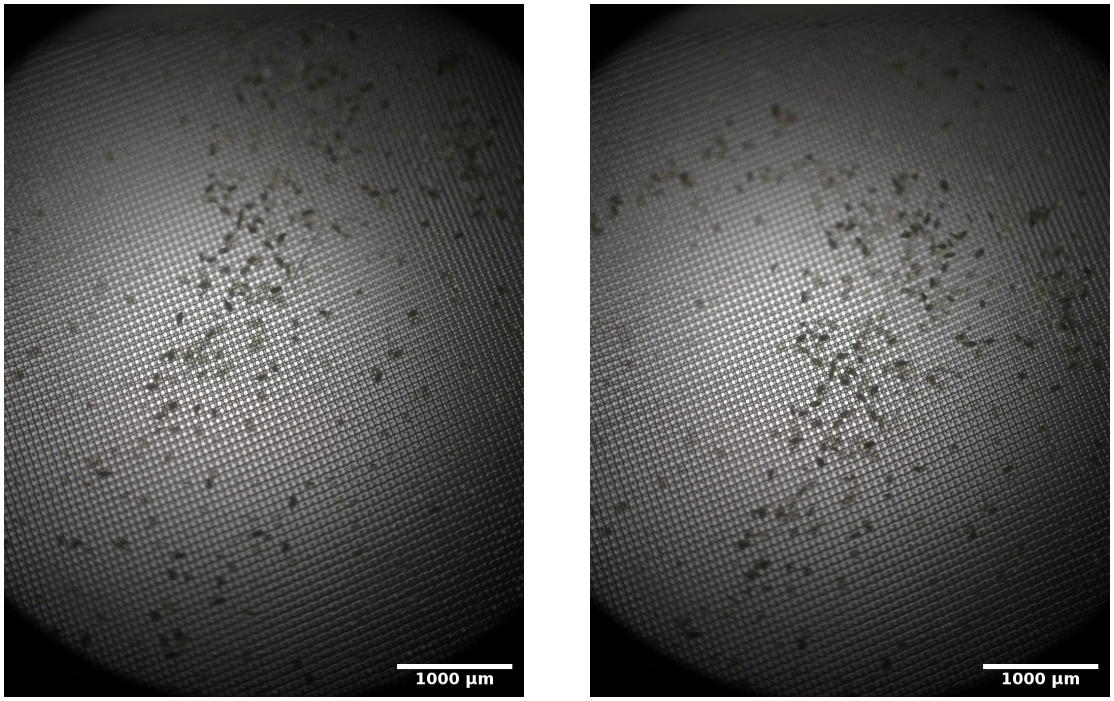

Figure 3-23: Images captured in 2018 using the mobile-phone reverse-lens microscope.

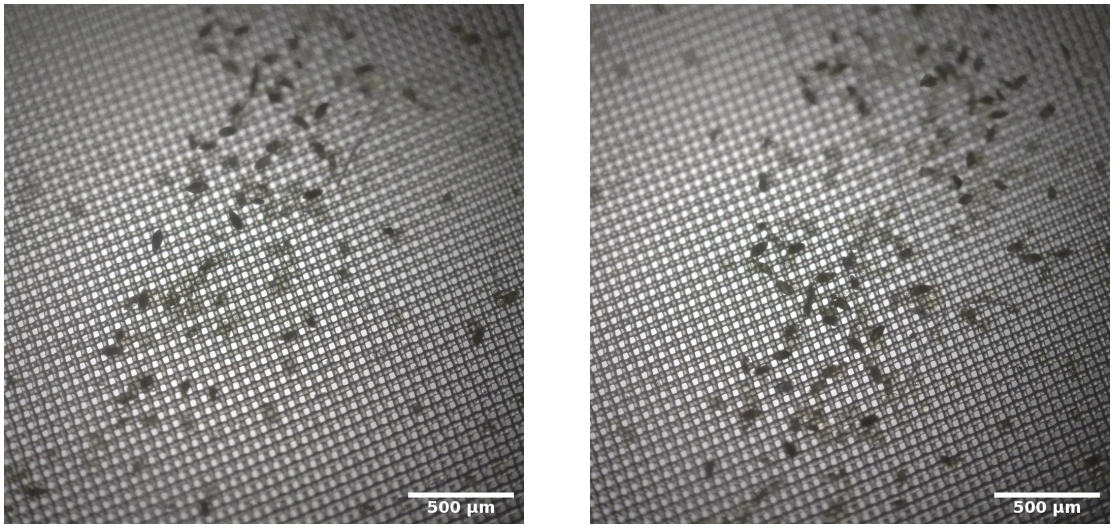

Figure 3-24: Cropped regions of the FoVs in Figure 3-23 used for developing detection algorithms.

3-2-2 Using the automated microscope with a Raspberry Pi camera

For this microscope to cover the entire standard filter of diameter 13 mm, a grid of images is required. Each image in the grid is one FoV. The expected grid size is 5×5, or 6×6 in the worst-case if some overlap is necessary for stitching the images and reconstructing the image of the entire filter. Each FoV, like the image in Figure 3-25, is of dimensions 3280×2464 pixels.

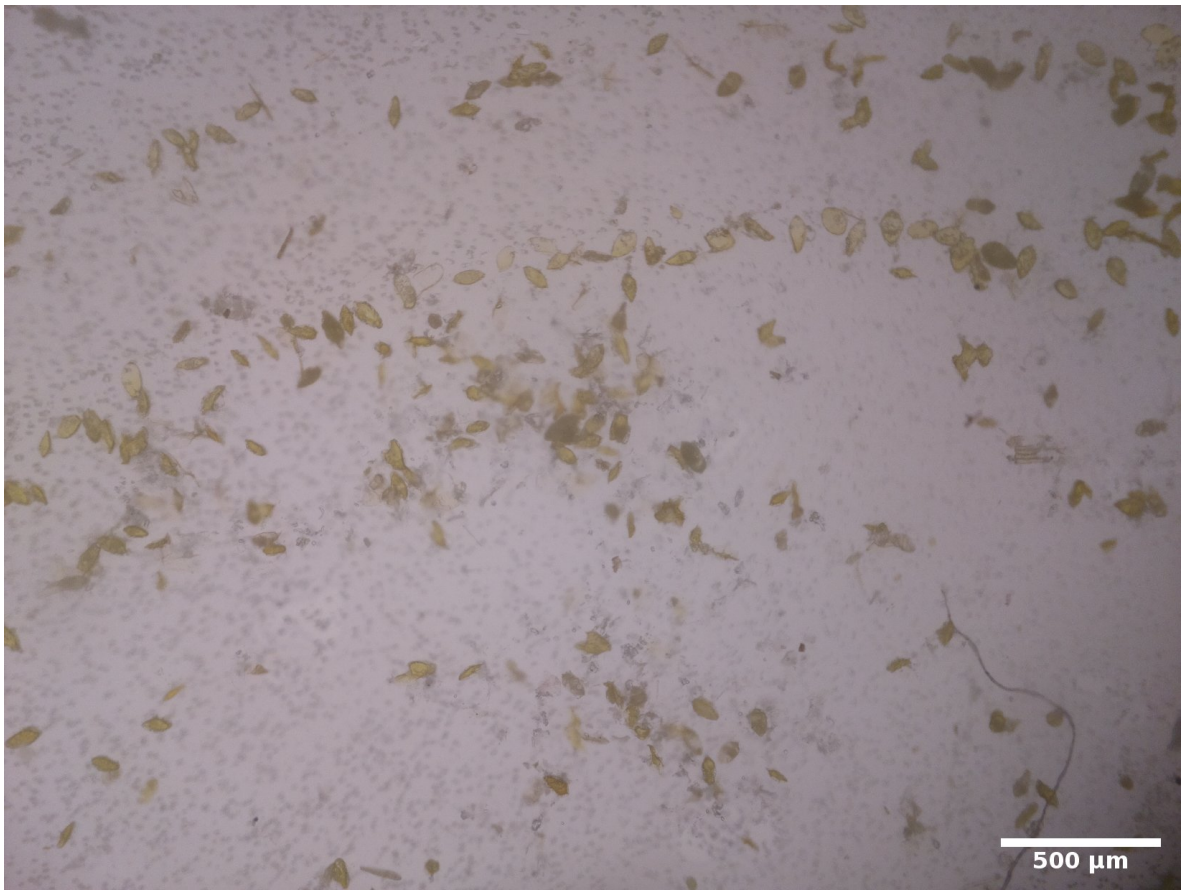

Figure 3-25: An FoV of the standard urine filter.

Improving the image quality is possible, by choosing a thinner diffuser sheet - currently 3 mm, lower thickness may yield better results - to let enough light to pass through, or by controlling the camera settings like the exposure, ISO, dynamic range and many others. The design of a low-cost alternative to a microscope condenser setup may improve the resolution of the system to an extent.

An essential requirement for the system is the detection of the starting point to image the standard filter with the filtrate. For this to work, in the automation phase, the system needs to identify the top or bottom end and either the left or right ends of the circular filter to begin the imaging process. Figure 3-26 shows the boundary at the right-side of the circular filter.

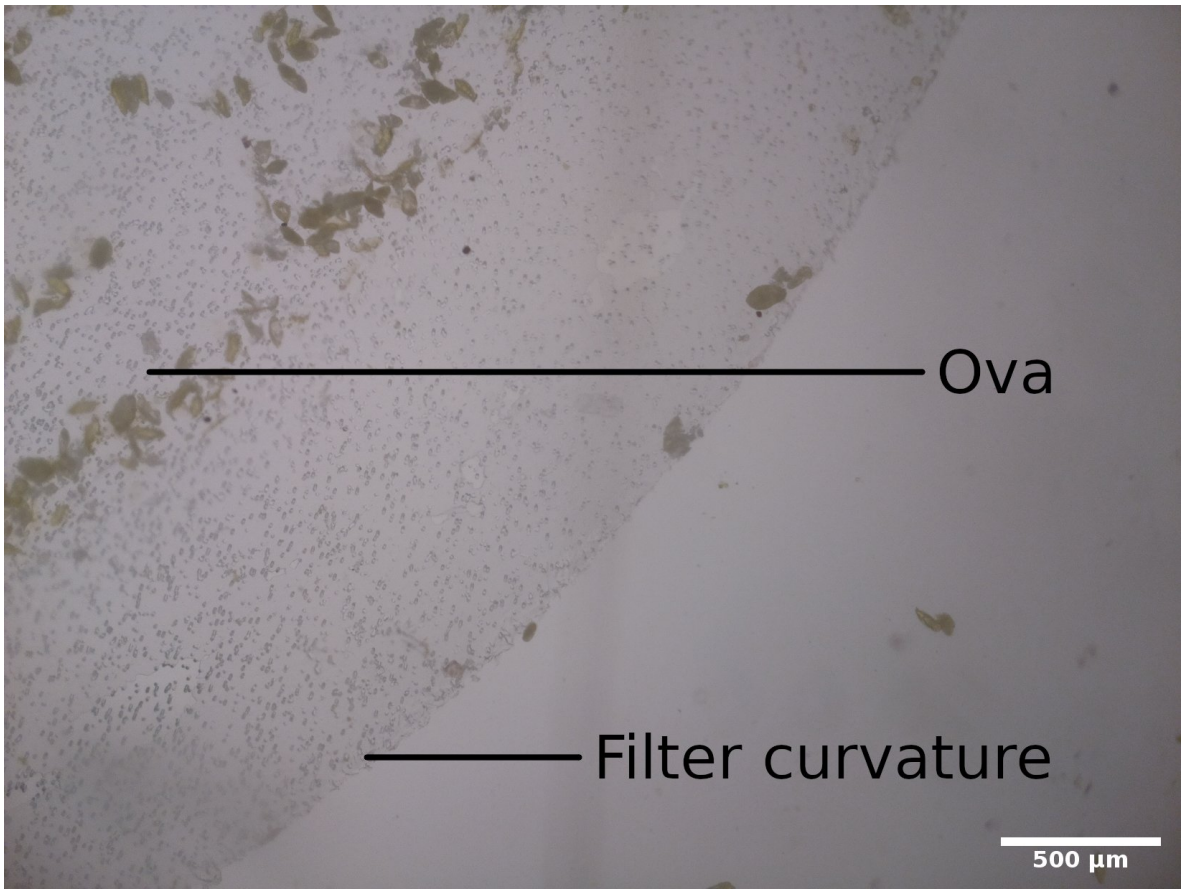

Figure 3-26: An FoV of the standard urine filter showing the curvature of the filter.

3-3 Detecting the *S. haematobium* ova

We developed the detection software only for the mobile-phone microscope, and the developement of the detection model and software for the automated microscope should be the focus of future research as there was limited time remaining for this thesis work. The automated microscope was a direct result of our critical evaluation of the mobile-microscope, which we discuss in Chapter 5.

3-3-1 Detecting ova using the mobile-phone microscope

Our goal is to model a detector using a few images, as shown in Figure 3-23 or 3-24, and evaluate the model on new pictures captured using the mobile-phone. We break the algorithm into two simple steps: localising the potential ova and classifying the potential candidates using a trained image classifier. We execute this implemented algorithm on a desktop/notebook computer, the phone and a Raspberry Pi 3B+ computer to evaluate and compare the performance.

Localising potential ova

For the description of the algorithm, we use the first cropped image in Figure 3-24 as the starting point. The original size of the image is 2048×2048. We scale it down to 1240×1240, which reduces the resolution but preserves sufficient features for analysis.

There are some ova among all the dark blobs in the image, and hence we aim to localise all the blobs. One can achieve this step using simple morphological operations, but the filter mesh in the background hinders this approach. So the first step is to explore methods to filter out the mesh. The mesh has a periodic structure of relatively high frequency in all directions, and hence we can eliminate the mesh using a low-pass filter (LPF) in the spectral domain, which is equivalent to a blur in the spatial domain [47].

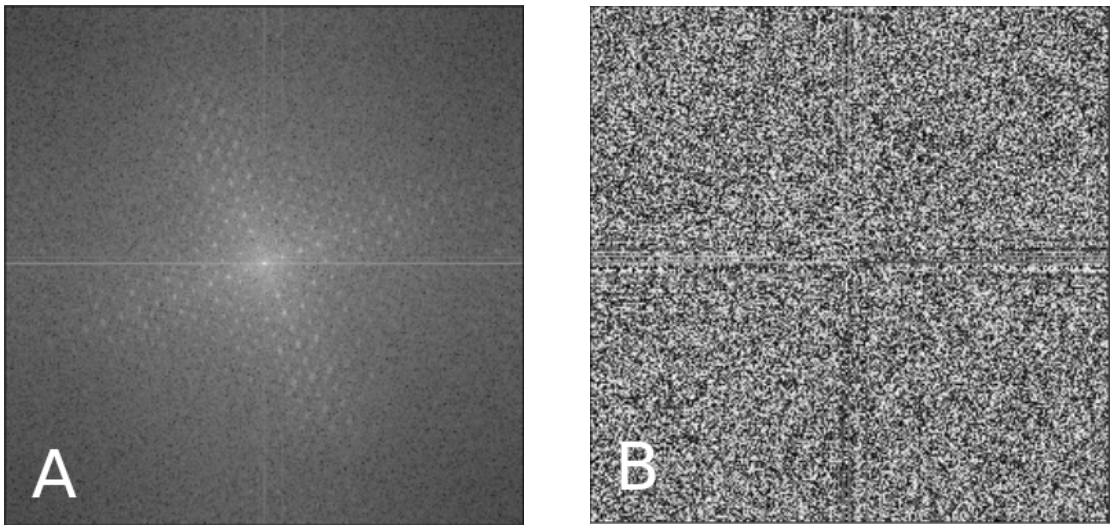

Figure 3-27: (A) The magnitude and (B) phase of the discrete Fourier Transform for the image under consideration.

Given a digital image $f(x, y)$, of size M $\times$ N, its 2-D discrete Fourier transform (DFT), F(u, v) - where u and v are the coordinates in the spectral domain - is given by [47]:

$$F(u,v) = \sum_{x=0}^{M-1} \sum_{y=0}^{N-1} f(x,y)\, e^{-j2\pi(ux/M+vy/N)} \tag{3-2}$$

Refer to Figure 3-27 for the resulting magnitude and phase images. We apply an ideal low-pass filter (ILPF) on the spectral data. Figure 3-28 shows the mask image representing the ILPF and the magnitude of the result of multiplying it with the spectral data.

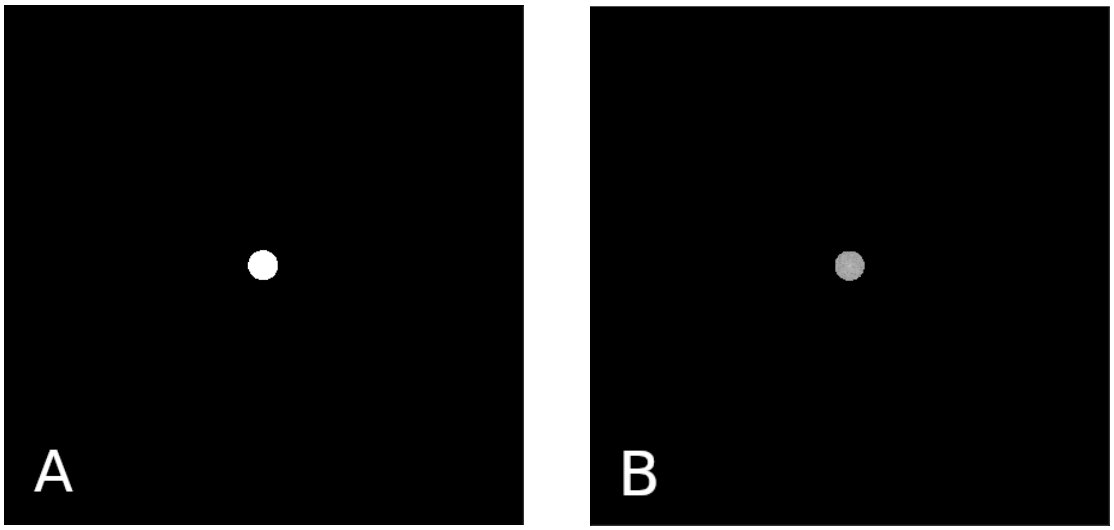

Figure 3-28: (A) The binary mask for the ILPF and (B) the magnitude plot of the masked DFT.

Using the resulting spectral data, we compute the inverse-DFT (IDFT) to obtain the filtered image in the spatial-domain, which we binarise using a threshold operation to separate the blobs from the background. The results are in the figure below.

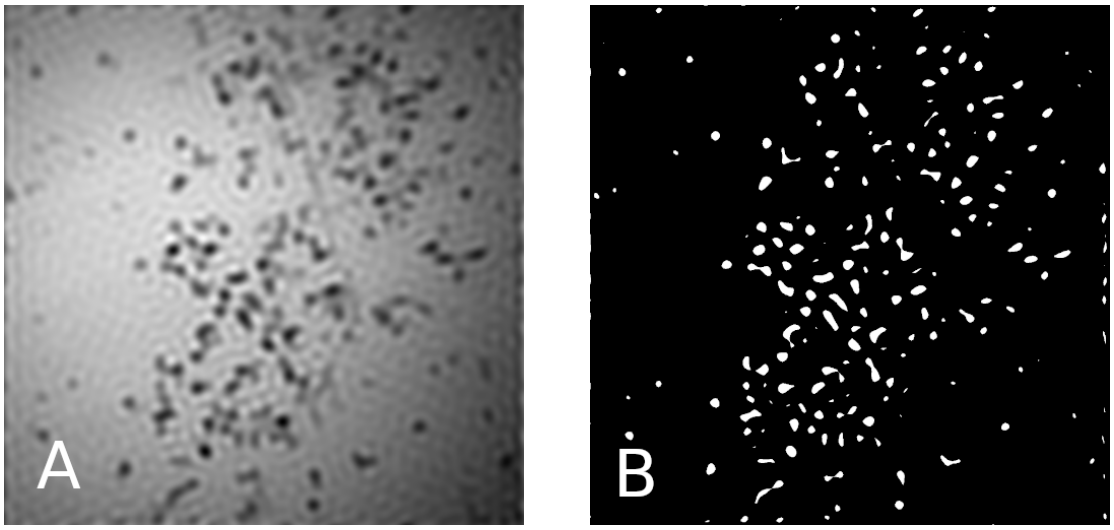

Figure 3-29: (A) The filtered image and (B) the resulting binary image.

From the binary image, we compute the contours and their respective bounding boxes for all the detected blobs and map this data to the original image.

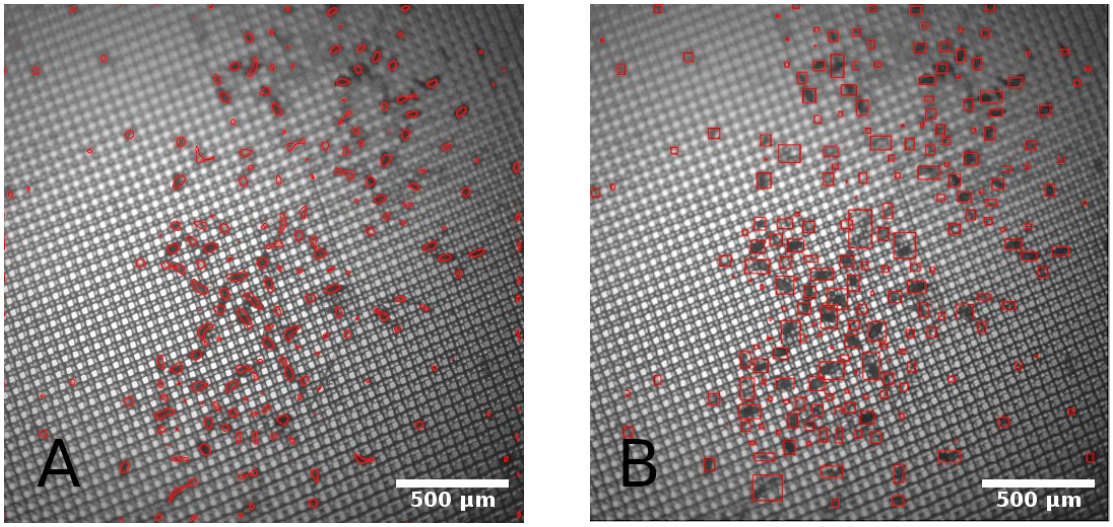

Figure 3-30: (A) The contours mapped to the original image and (B) the computed bounding boxes of all the detected blobs in the threshold image.

Using the bounding box data, we estimate the coordinate of the centre for each blob. We crop regions of size 64×64 using the obtained centres. The final step for detection uses the cropped regions as inputs to an image-classifier.

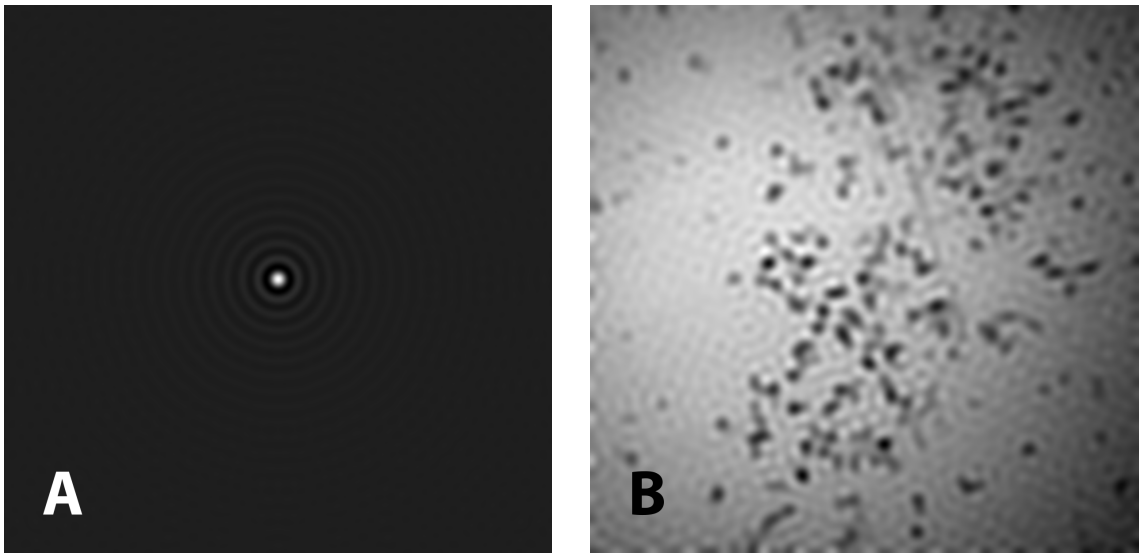

Figure 3-31: (A) The IDFT of the ILPF mask image shown in Figure 3-28A. The result is a sinc function. (B) The result of convolving the original sample image using (A) as the kernel. Note that the result is the same as in Figure 3-29A, obtained by frequency-domain filtering.

Before describing the classification step, we quickly mention the equivalent operation in the spatial domain, for the frequency domain filtering, which is a convolution with a relevant

kernel. However, the precise kernel matrix is directly dependent upon the periodicity of the mesh, the pore size etc. which we analyse in the spectral domain. A general solution is to use the most conservative blur that preserves details of the ova (the blobs), irrespective of the pore size. The kernel for blurring by convolution in the spatial domain is the IDFT of the ILPF mask image shown in Figure 3-28A, which is the sinc function. Refer to Figure 3-31 for the results of this procedure. There is no significant difference in performance (execution time) between the two approaches, for the utilised image sizes.

Classifying the potential ova

We train and utilise a binary classifier to segregate the regions of interest into two classes - *ovum* and *not ovum*. For training we built a dataset by cropping 120 regions for each class from two images of urine samples, each of dimensions 1240×1240, which were annotated with the help of an expert. The image considered for the current description of the analysis did not contribute to the training data. Figure 3-32 represents nine sample points from each class. Each data point is a 2D matrix - grayscale - of dimensions 64×64.

The original images registered using the mobile are colour images. Due to the lack of colours from observation, we convert them to grayscale images before processing. We augmented the dataset to inflate it artificially, using label-preserving transformations [48]. Specifically, we used rotations - by 90°, 180° and 270° - and the transpose of each of the four orientations. This step increased the dataset size to eight times the original size, from 120 images to 960 images in each class.

For the classifier we use a Support Vector Machine (SVM), precisely the C-Support Vector Classification (C-SVC) model [49, 50], with a linear kernel. The data is first normalised to the range $[0, 1]$. We shuffle the entire dataset and split it into a training and test set containing 70% (672 images per class) and 30% (288 images per class) of the original data respectively. The normalised pixel data - 4096 pixels for the 64×64 images - are the features for the classification model. The used training functionality for the SVM classifier is from the *scikit-learn* [51] machine learning library. On a desktop machine with an Intel i7 7700HQ (@ 2.80 GHz) processor and 16 GB of memory, the average training time is 4.5 seconds. The trained model demonstrated an accuracy of 96%.

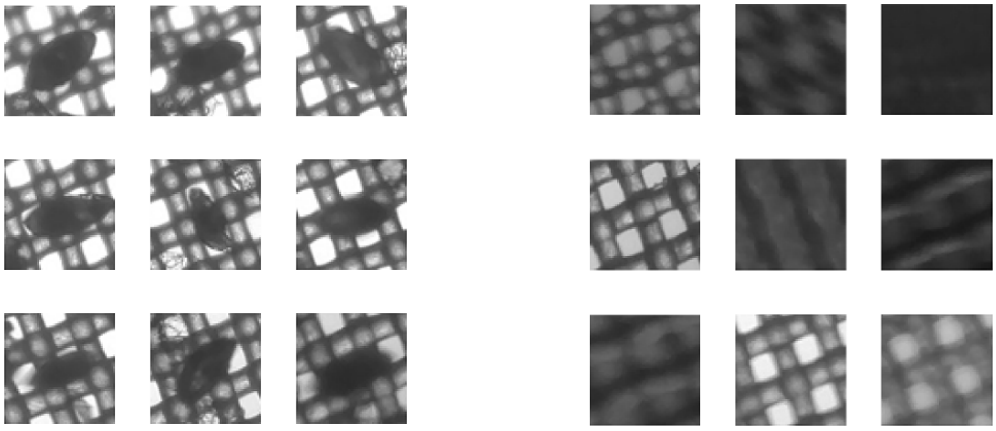

Figure 3-32: Data points representing (Left) the *ovum* class and (Right) the *not ovum* class.

In the detection pipeline, after obtaining the coordinates of the potential ova from the localisation step, the procedure is programmed to vectorise - 64×64 matrices are transformed to a 4096×1 vector by concatenating the rows - and feed the normalised images to the SVM classification model. The output of the classifier is either a zero (0) or a one (1), representing the classes *ovum* and *not ovum* respectively.

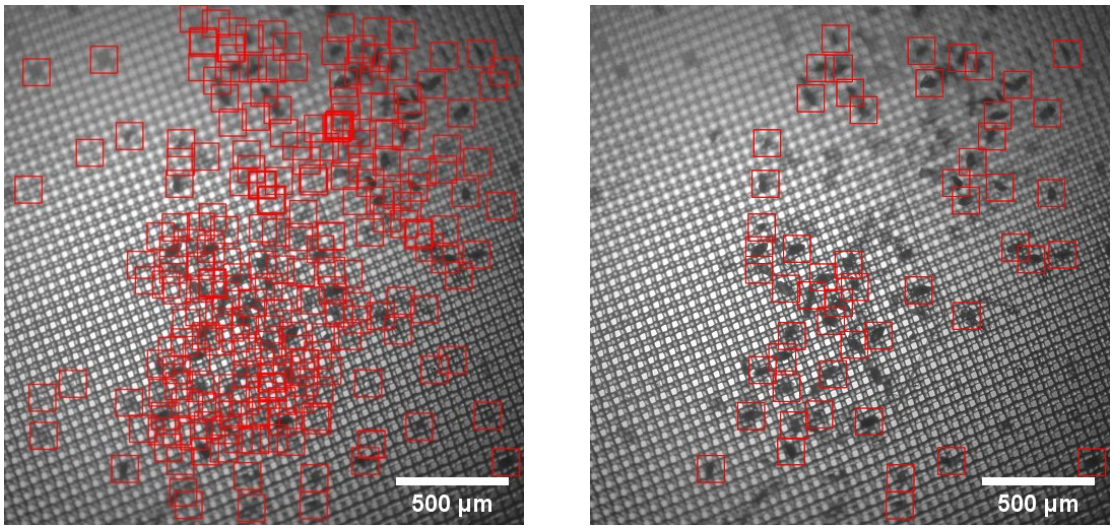

Figure 3-33: (A) Bounding boxes for the potential ova, and (B) the result of classification.

The purpose of the discussed SVM classifier was to demonstrate a simple classification model for the system. One can use other competent models, like a classifier based on convolutional neural networks (CNN). It is also possible to replace the entire detection pipeline with a deep-learning-based object detector at the cost of increased computation time.

Implementation and performance

To prototype the algorithm, we used the OpenCV library [52] for the image-processing steps, in the Python programming language. We evaluated the procedure on three different platforms: a desktop/notebook computer, the Moto X Style mobile-phone and the Raspberry Pi 3B+ computer. We used the Raspberry Pi 3B+ instead of the newer 4B model because this experiment predates the release of the newer version. We wrote the relevant software ports for the different platforms and measured the average execution time. Refer to Appendix A for the source code. The summary is tabulated below.

Computer	Language	Execution time
Intel i7 7700HQ @ 2.8 GHz (Fedora 29 - Linux)	C++	0.24 s
Moto X Style (2015) (ARMv8-A) 64-bit @ 1.8 GHz	Java for Android	5.0 s
Raspberry Pi 3B+ (ARMv8) 64-bit @ 1.4 GHz	C++	6.2 s

Table 3-4: Performance of the described algorithm on the three mentioned platforms.

The measurements in Table 3-4 are independent of the available system to image the ova. That is, we measure the execution time, assuming the images for analysis are already available. Diagnosis time, on the other hand, will also account for the time to prepare and scan the filtered sample. We note that the execution time is adequate to analyse the sample quickly using the phone, although by filtering urine over a smaller area.

Let us discuss some limitations of the current procedure.

1. Note that all the ova in the images from the phone are dark black. This colour may be due to the cultured sample being old at the time of the experiment, but this fact requires definite confirmation from experts and the literature. Because of the dark ova being present, we ignored staining the sample using Lugol's Iodine. We also ignored many other steps from the standard protocol. In practice, most of the ova are translucent.
2. The development of the algorithm, for the proof-of-concept, focused on simplicity and reducing the computational load for portable computers. Intermediate steps will be necessary to make the procedure more robust. For example, in the blob detection step, two or more ovum can overlap in the scene. This event will result in either the truncation of the big blob or detection of one ovum in the region of interest. The addition of a relevant segmentation procedure can help overcome this possibility.

3. The resulting image shown in Figure 3-33B contains a few false-positives (targets that are not ova but identified as ova) and false-negatives (targets that are ova but not identified) to question the overall reliability of the procedure for automated medical diagnosis. Validation is possible only with the analysis of many more samples, preferably using schistosomiasis-positive urine samples from the field.

3-3-2 Detecting ova using the automated microscope

The development of a detection model for analysing the images captured using the automated microscope is a primary goal for the next phase of the project. The focus should be on developing and optimising a computer vision model, for ova detection, for deployment on a low-powered computing device like the Raspberry Pi 4B. To begin the development of this model, a dataset collected using this device is required.

Chapter 4

Experimental Results

To publish results on the classifier's performance, and the diagnostic sensitivity and specificity, testing with a large number of samples is necessary. The few samples analysed using the mobile-phone microscope were cultured samples of *S. haematobium* ova obtained from the parasitology research lab at LUMC, Leiden. The acquired images were insufficient to compute metrics of significance. We captured four images with observable eggs, and built a training set for the SVM classifier from two of these images. We used the other two images for testing the classifier. Refer to Figure 4-1 for the detection results on the test images.

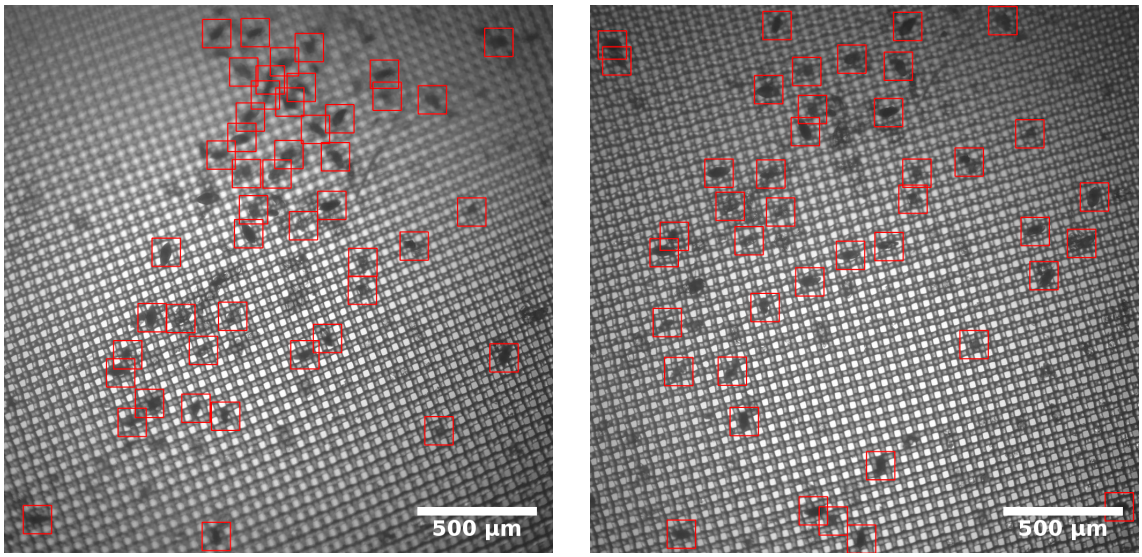

Figure 4-1: Detection results on the two test images.

To evaluate the design choices of the mobile-phone microscope and compute the relevant statistics representing the performance of the device in the field, we organised a visit to the *ANDI Centre of Excellence for Malaria Diagnosis* at the College of Medicine, University of

Lagos, Nigeria. The objective was to filter schistosomiasis-positive urine samples, instead of lab cultured ones, and capture images of the residue for each sample. Using infected urine samples simulates sample testing conditions in the field, and enables to observe how the cloth filters perform in the presence of the ova and other contents in the urine - cells, proteins, white blood cells, blood, bacteria etc.

4-1 Testing with schistosomiasis-positive urine samples

An expert microscope operator at Lagos, Nigeria, trained specifically for schistosomiasis infections, executed tests with schistosomiasis-positive urine using our small and inexpensive cloth filters. To ease the filtering of urine using a syringe, the design engineers collaborating with us developed reusable plastic caps for mounting the mesh and placing the cap on top of a sample holder, as shown in Figure 4-2A. For comparison and documentation of the process, the operator filtered the same samples using the standard protocol as well. The employed devices were our mobile-phone microscope for the cloth filters and a conventional microscope for the standard filters with a 13 mm diameter. The execution of the standard procedure progressed very efficiently. For the research work encompassing smart diagnostics for schistosomiasis, observing this procedure helped in documenting and understanding the benefits and pitfalls. A few of these insights are mentioned in Chapter 2 of this thesis.

With the mobile-phone microscope, the expert was able to identify an egg or two by manual inspection. The overall performance of the instrument was subpar. The current design for filtering the urine using a syringe requires pressing the syringe tip directly on top of the working area of the cloth, which rendered the filtering procedure hard. Figure 4-2B shows a user attempting to filter the urine sample using the mentioned caps. On passing about $2-4$ ml of a sample, urine sediments covered the cloth making further filtering difficult, and the application of more pressure lead to its deformation.

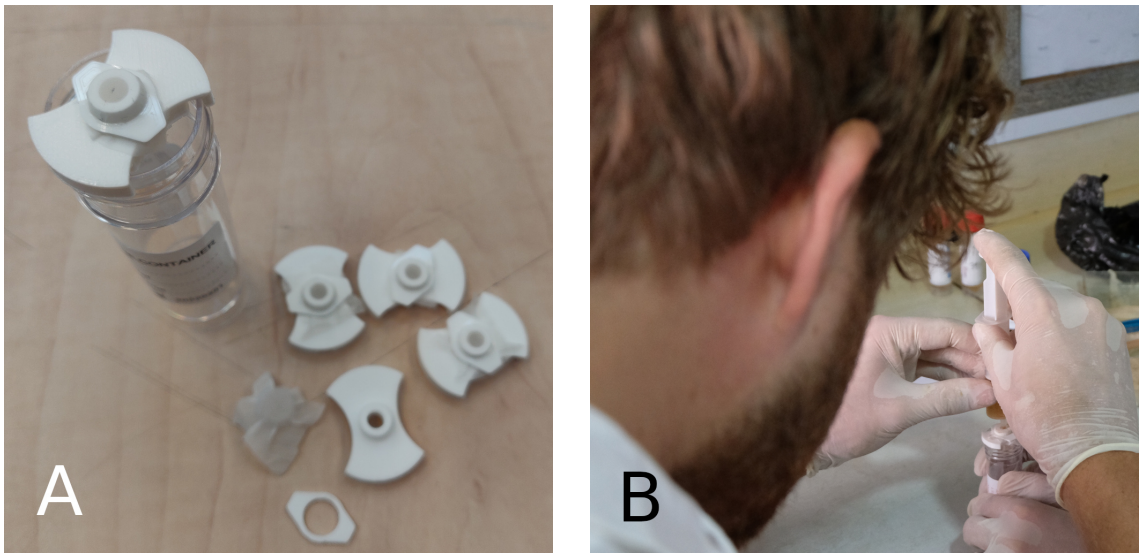

Figure 4-2: (A) Custom designed filter caps that can be mounted on a sample tube. (B) A user attempting to filter a urine sample through the filter cloth using a syringe.

The results demonstrate the inadequacy of the filters with a small area for filtering the standard amount of urine sample, which if you recall is 10 ml. In fact, the area due to the thickness of the syringe outlet covered a significant portion of the filter cloth, making all of this area unworkable. As a result, the urine sediments were clumped in the middle, which is evident from the images shown below in Figure 4-3.

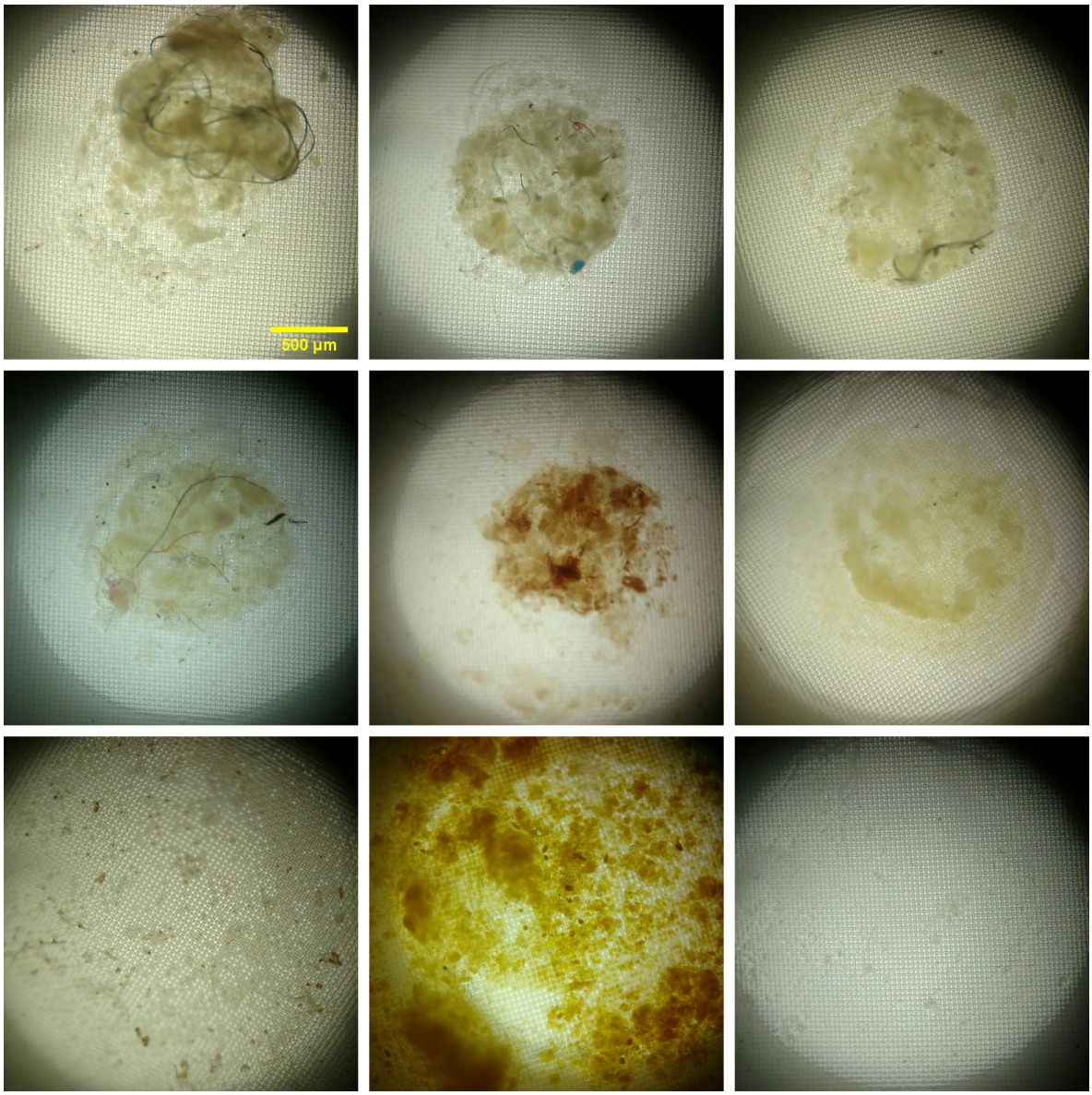

Figure 4-3: Nine images of sediments from partially filtered - less than 10 ml - urine samples.

The detection model described in Section 3-3 did not detect the ova - shown in Figure 4-4B - that were manually identified by the operator. Recall that the procedure first converts the captured images to grayscale before processing, because our experiments using cultured samples furnished images with dark black ova. However, the ova shown in 4-4B were translucent to begin with, and developed an orange-brown tint when stained using Lugol's Iodine solu-

tion. The ovum at the top in the image also displays some opacity, and for this reason it is understandable for the trained classifier to classify the ovum as a negative. Further analysis is required to diagnose why the model did not detect the second ovum at the bottom of the image.

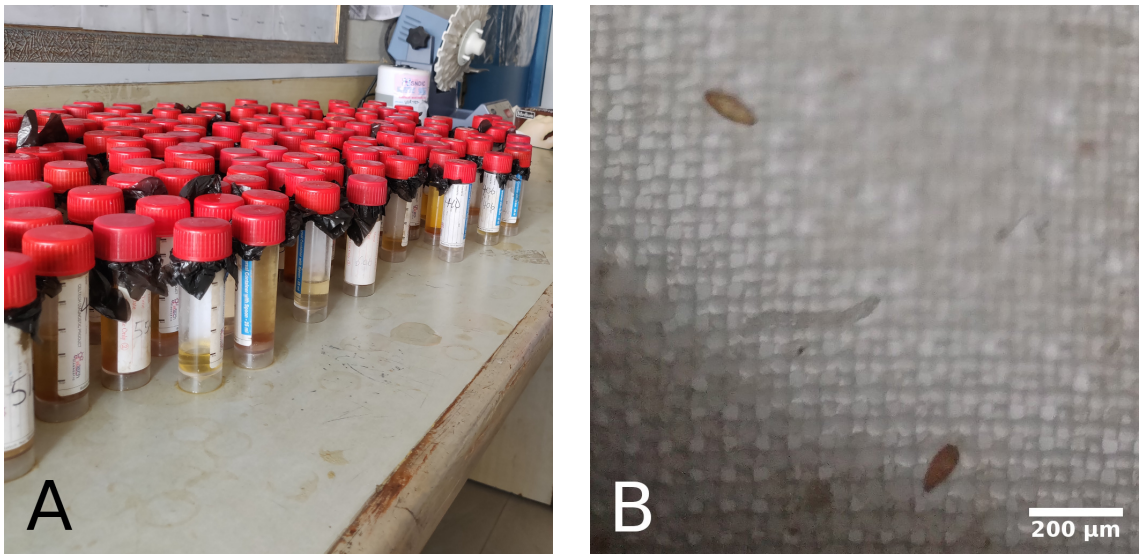

Figure 4-4: (A) Schistosomiasis-positive urine samples lined up for assessment in the lab at *ANDI Centre of Excellence for Malaria Diagnosis*, Lagos, Nigeria. (B) The image with the two ova detected by the microscope operator using our mobile-phone microscope.

Chapter 5

Discussion

5-1 Recommendations for the mobile-phone microscope

As reported in Chapter 4 - concerning the experimental results - the designed mobile-phone microscope system did not provide the expected results, primarily because of issues in the design of the urine filtering components. The results do not indicate any drawbacks with the optical system in this device. Therefore, with research dedicated towards the development of an improved and practical filtering kit, the mobile-phone microscope is still promising for use in point-of-care diagnosis.

Recall that the filtering of the urine sample by placing the syringe directly on top of the cloth resulted in rapid clogging by urine sediments, in the centre of the filtering area. This event rendered a significant area of the filter ineffective. An improved design allowing filtration with the syringe positioned away from the cloth by a small distance may provide better results. It is also possible to circumvent the issue of clogging by filtering the 10 ml of urine through many small cloth filters and analysing them individually, at the cost of increased workload.

Using the same mobile-phone, increasing the diameter of the fabric for filtering will not yield better results because the limited area of the camera sensor cannot image the entire FoV in a single-shot. Translating the filtered sample will be necessary. A possible solution is to increase the size of the cloth filter to have its radius equal in length to the diagonal of the camera sensor and spin the filter about its centre, similar to the mechanism of an optical storage drive. Refer to Figure 5-1 for an illustration of the proposal. If this solution is worth exploring, it may prove useful to use the standard filter membranes - with a diameter of 13 mm - and use a mobile-phone whose camera sensor has a diagonal length of at least the radius of the filter membrane. Coincidentally, the mobile-phone we used - the Moto X Style 2015 - has a sensor size of 5.985×4.497 mm, which corresponds to a diagonal of length 7.48 mm! Recently, we evaluated another mobile-phone - the Redmi Note 7 - which has the same pixel size of 1.12 μm, but a sensor of diagonal length 8 mm. Recent advances in sensor technology led to the development of sensors like the SONY IMX686, which has a pixel size of 0.8 μm and a sensor of diagonal length 9.3 mm. The last two sensors can certainly image the entire standard filter

membrane with the described concept. Stitching the acquired images is not straightforward because it is necessary to account for lens distortions and pixel overlap. However, stitching is not required to diagnose and quantify the infection.

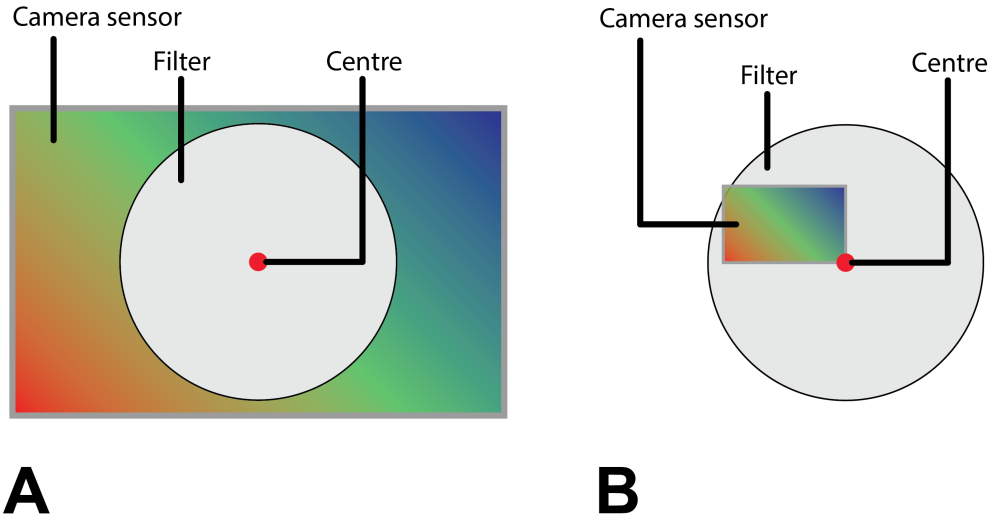

Figure 5-1: (A) The current mobile-phone microscope concept. In this case, the filter is the low-cost fabric material small enough to fit within the area of the camera sensor. (B) The suggested concept uses the standard filter membrane (diameter 13 mm) and a camera sensor whose diagonal length is at least as long as the radius of the filter. Spinning the filter about its centre enables recording its entire surface.

5-2 The automated microscope design

The primary motive for developing this microscope is to deploy, in the short-term, an instrument that is inexpensive and automates the recognised diagnosis and quantification method set forth by WHO. There are higher chances for the medical community to adopt such a device than one that replaces the sample preparation procedure. The current technological state of the device is, it allows manually capturing images of the filtered sample over the filter with a diameter of 13 mm.

Field reports and the WHO manuals for a health lab also mention a filter of diameter 25 mm. The only changes needed in the device to incorporate these filters are in the design of the sample holder, which moves along the Z-axis. The camera, which operates along the X and Y axis, is already capable of traversing the entire area of the larger filter. The design details and choice of components - including the motors, camera and on-board computer - are not final. It is crucial to determine the availability of the relevant components, and if not, replace the parts with ones that are accessible in the context of deployment. With the open-source philosophy in mind, for the proof-of-concept, the design incorporates open-source and community-supported hardware - the Raspberry Pi computer and the Raspberry Pi camera. The primary motivation for this choice is the presence of a large community of engineers backing development and online support for this platform, which makes it simple to modify

or extend the system for a relevant context.

The optical system described in Section 3-1-1 consists of the Raspberry Pi camera as a whole unit, and a lens of the Raspberry Pi camera positioned in reverse to produce a microscope of magnification $\times 1$. The images captured with this system show the ova with an adequate resolution to identify them. However, a thorough evaluation by expert parasitologists is necessary to establish this fact. The terminal spine, which is the characteristic feature a microscope operator looks for, is visible only for few of the ova in our images. Our current suggestion is, the optical resolution should be improved to reveal more details of the ova. This improvement is attainable by increasing the amount of light available underneath the diffuser, reducing the thickness of the diffuser sheet by a small amount, optimising the sample illumination setup to direct more light, and using a camera with a smaller pixel size.

In the long-term, exploring the use of standalone mobile-phone camera units may prove fruitful. Newer camera modules have a sub-micron pixel size, a larger sensor area, and f-numbers of 1.9 and 1.8. However, programming these modules as standalone units is not straightforward. For a proof-of-concept demonstration, building a mobile-phone microscope using a mobile-phone with the relevant sensor will suffice. Table 5-1 lists the pixel and sensor sizes of three state-of-the-art sensors used in mobile-phones.

Model	**Pixel size**	**Sensor size**
SONY IMX677	1.12 μm	6.270×4.729 mm
SONY IMX686	0.80 μm	7.398×5.555 mm
SAMSUNG ISOCELL Bright GW1	0.80 μm	7.42×5.555 mm

Table 5-1: Relevant specifications of newer CMOS sensors used in mobile-phones.

5-3 Next steps for our instrument

In this section, we state the necessary requirements to achieve the technology level for evaluation and deployment of our $\times 1$ microscope in a relevant contexts. Presently, the instrument is only capable of imaging the *S. haematobium* ova by manual operation, but the objective is to automate the process of imaging and analysing the prepared samples.

The system is equipped with the relevant hardware for achieving the required level of operation. The modules that are incomplete or require development are the control software modules, viz. the auto-focus, detecting the boundary of the filter membrane, traversing the camera across the sample for scanning, and detecting the ova for diagnosing and quantifying the infection. With these features installed, subsequent steps are to demonstrate and get confirmation from experts on the quality of the images for diagnosis and quantification. This step will provide the necessary feedback for optimising the device to improve the image quality, performance, and the user interaction. Parallelly, scanning a large number of samples, quantifying them using a microscope and annotating the images obtained using the developed device, with the cooperation of an expert is vital. This process will enable the construction of a large dataset for analysis, and the development of a relevant object detection pipeline to automate the diagnosis and quantification steps for use in the field.

One of the motives for adopting a mobile-phone microscope was the possibility of registering analysed samples and uploading the data to a medical records database. A feature like this will assist and boost disease mapping procedures, enabling medical organisations and associations to mobilise the necessary interventions for control and elimination programs effectively. The presence of a computer in the instrument makes it possible to add more sophisticated features for tele-medicine, like real-time remote analysis by an expert from a distant lab. However, such technologies require consistent network access, which is currently limited in the context areas.

Chapter 6

Conclusions

The initial proposal for this work was to show the potential of using a reverse-lens mobile-phone microscope integrated with computer vision software to diagnose and quantify urinary schistosomiasis. However, realising this objective with the implemented design and custom sample preparation protocol revealed problems - small filter area resulting in a limited area for filtration, clogging of the filter by urine sediments, and ensuring the filter fabric is taut - after testing with schistosomiasis-positive urine samples from the field. The discussed issues are more relevant for quantification since the only requirement for diagnosis is the identification of at least one ovum. With some deliberation after examining the results, we lead the development of a device which does not alter the established sample preparation procedure, and images the filtered urine sample over multiple FoVs. In other words, the new design was an automated microscope.

This instrument has a magnification of $\times 1$, was built to provide reliable performance while keeping the manufacturing simple and inexpensive. We presented a potential method for operating the stepper-motors without the use of calibration switches. The present costs to procure the materials, manufacture structural components using 3D printing and laser-cutting, and assembling the device are under €200. Although full-automation or diagnostic assistance are the intended applications, the current device can only capture the images of the filtered urine samples by manual operation. The missing features to complete the device are the auto-focus software, automatically detecting the boundary of the urine filter, imaging the entire filtered sample, and executing an object detection procedure for diagnosis and quantification. Further optimisations will be necessary, for this device, based on evaluations with the help of expert operators and parasitology researchers. After the manifestation of all these specifications, analysing a large number of infected urine samples will be necessary to validate the concept and report on the relevant statistical metrics.

6-1 Final note

In 2012, the launching of a collaborative disease eradication programme called the *London Declaration on Neglected Tropical Diseases* took place. It was a coordinated agreement between participating public and private sectors to control or eliminate at least ten diseases from a list of NTDs by 2020. Concerning schistosomiasis, the goal was to "sustain, expand and extend drug access programmes to ensure the necessary supply of drugs and other interventions to help control by 2020" [53]. Funding the research led to a significant understanding of the disease, and the development of novel approaches for diagnosis. We are now in the year 2020, and schistosomiasis still affects $200 - 250$ million people. Although novel diagnostic and quantification approaches that do not require a lot of equipment and forgo sample preparation are an ideal requirement, it makes sense to use them on a large scale when the cost per diagnosis is affordable. Until then, we are confident that an instrument like the one presented in this work can serve in diagnosing and mapping the diseases in remote areas lacking adequate means.

Appendix A

The Algorithm for Ova Detection

The following source code is(are) for the urine sample filtered using the inexpensive fabric filter used with the mobile-phone microscope.

A-1 Algorithm in Python

A-1-1 detect.py

```
1  import cv2
2  import numpy
3  from sklearn.svm import SVC
4
5  # Load the pre-trained SVM model from scikit's sklearn library
6  # using a preferred method (pickling, numpy, etc)
7  classifier =
8
9  # Open the image
10 raw_image = cv2.imread('PATH_TO_IMAGE', cv2.IMREAD_GRAYSCALE)
11
12 # Compute the DFT
13 fft_img = numpy.fft.fftshift(numpy.fft.fft2(raw_image))
14
15 # Create an ideal LPF
16 mask = numpy.zeros(fft_mag.shape)
17
18 i_r = 36            # Internal radius of the LPF circle
19 i_r_sq = i_r**2
20 y_center = mask.shape[0] / 2
21 x_center = mask.shape[1] / 2
22
23 for x in range(mask.shape[1]):
24     for y in range(mask.shape[0]):
```

```
25
26          dist_sq = (x - x_center)**2 + (y - y_center)**2
27
28          if (dist_sq <= i_r_sq):
29              mask[y, x] = 1
30
31  # Mask and IDFT
32  masked_fft = numpy.multiply(fft_img, mask)
33  new_fft_inv = numpy.fft.ifft2(numpy.fft.ifftshift(masked_fft))
34  filtered_image = numpy.real(new_fft_inv) # Take the real part
35
36  # Normalise pixel levels
37  filtered_image = cv2.normalize(filtered_image, None \
38      , alpha=0, beta=255, norm_type=cv2.NORM_MINMAX, dtype=cv2.CV_8U)
39
40  # Apply threshold
41  thresh_img = cv2.adaptiveThreshold(filtered_image, 255 \
42      , cv2.ADAPTIVE_THRESH_GAUSSIAN_C, cv2.THRESH_BINARY_INV, 49, 10)
43
44  # Detect contours
45  _, contours, _ = cv2.findContours(thresh_img \
46      , cv2.RETR_EXTERNAL, cv2.CHAIN_APPROX_SIMPLE)
47
48  # Detect centres of potential ova
49  LEFT_X = 0
50  RIGHT_X = WIDTH - 32
51  TOP_Y = 0
52  BOTTOM_Y = HEIGHT - 32
53
54  centres = []     # Empty list to store centres
55
56  for i in range(len(contours)):
57      x, y, w, h = cv2.boundingRect(contours[i])
58
59      if (x > LEFT_X and x < RIGHT_X and y > TOP_Y and y < BOTTOM_Y):
60          centres.append((x + w/2, y + h/2))
61
62  # Classify and draw boxes of predictions
63  final_img = raw_image.copy()
64  final_img = cv2.cvtColor(final_img, cv2.COLOR_GRAY2RGB)
65
66  NUM_EGGS = 0
67  for c in centres:
68      img = raw_image[c[1]-32: c[1]+32, c[0]-32: c[0]+32]
69
70      img = (numpy.expand_dims(img, 0))
71
72      try:
73          prediction = numpy.argmax(MODEL.predict(img)[0])
74
75          if prediction == 1:
76              final_img = cv2.rectangle(final_img, (c[0]-32 \
77                  , c[1]-32),(c[0]+32, c[1]+32), (0, 255, 0), 2)
```

```
78              NUM_EGGS += 1
79
80      except ValueError:
81          # Do nothing for now
82          print "ValueError for", c
```

A-2 Algorithm in C++

Makefiles are ignored. Build and test in a preferred development environment.

A-2-1 util/eggidentify.h

```
1  #include <opencv2/core.hpp>
2
3  #ifndef _EGG_IDENTIFY_
4  #define _EGG_IDENTIFY_
5
6  class EggIdentify
7  {
8
9  private:
10   cv::Mat raw_image;
11   cv::Mat process_image;
12   cv::Mat user_image;
13   cv::Mat threshold_image;
14   cv::Mat erosion_kernel;
15
16   // Resources for contours detection.
17   std::vector<std::vector<cv::Point>> contours;
18   std::vector<cv::Vec4i> hierarchy;
19
20   // Resources for contour centres.
21   std::vector<cv::Point2d> ctr_centres;
22
23   void prepare_images(void);
24   void determine_contour_centres(void);
25
26 public:
27   const static int RAW_IMAGE = 0;
28   const static int PROC_IMAGE = 1;
29   const static int USER_IMAGE = 2;
30
31   EggIdentify();
32
33   void capture_image(void);
34   void show_img(int);
35   void run(void);
36 };
37
```

```
38 #endif
```

A-2-2 util/eggidentify.cpp

```
1  #include <opencv2/opencv.hpp>
2  #include <opencv2/core/core.hpp>
3  #include <opencv2/imgproc.hpp>
4  #include "opencv2/highgui.hpp"
5
6  #include <string>
7
8  #include "eggidentify.h"
9
10 EggIdentify::EggIdentify()
11 {
12     // Initialize the erosion kernel.
13     erosion_kernel = cv::getStructuringElement(cv::MORPH_RECT, cv::Size
           (5, 5));
14
15     // Initialize the vector of Point2d for contour centres.
16     ctr_centres = std::vector<cv::Point2d>();
17 }
18
19 void EggIdentify::capture_image(void)
20 {
21     // Currently reading an image from the storage.
22     raw_image = cv::imread("../../images/regions/02.jpg", cv::
           IMREAD_GRAYSCALE);
23
24     // Add code to retrieve the image from the camera.
25
26     prepare_images();
27 }
28
29 void EggIdentify::prepare_images(void)
30 {
31
32     process_image = raw_image.clone();
33
34     cv::cvtColor(raw_image, user_image, cv::COLOR_GRAY2BGR);
35 }
36
37 void EggIdentify::show_img(int img_code)
38 {
39
40     std::string win_name = "";
41
42     switch (img_code)
43     {
44     case EggIdentify::RAW_IMAGE:
45         win_name = "Raw image";
46         cv::namedWindow(win_name, CV_WINDOW_NORMAL);
47         cv::imshow(win_name, raw_image);
```

```
48          break;
49
50      case EggIdentify::PROC_IMAGE:
51          win_name = "Process image";
52          cv::namedWindow(win_name, CV_WINDOW_NORMAL);
53          cv::imshow(win_name, raw_image);
54          break;
55
56      case EggIdentify::USER_IMAGE:
57          win_name = "User image";
58          cv::namedWindow(win_name, CV_WINDOW_NORMAL);
59          cv::imshow(win_name, raw_image);
60          break;
61
62      default:
63          break;
64      }
65
66      if (win_name != "")
67      {
68          cv::resizeWindow(win_name, 800, 800);
69      }
70
71      cv::waitKey(1);
72  }
73
74  void EggIdentify::determine_contour_centres(void)
75  {
76      const int EDGE = process_image.rows;
77      const int EDGE_M_1 = EDGE - 1;
78
79      // Initialize the mask image.
80      // CAN BE INITIALIZED IN ADVANCE (IF EDGE IS KNOWN).
81      cv::Mat mask_image = cv::Mat::zeros(process_image.size(), CV_32F);
82
83      const int r = 36;
84      const int r_sq = r * r;
85
86      for (int x = 0; x < r; x++) {
87          for (int y = 0; y < r; y++) {
88
89              if ((x*x + y*y) <= r_sq) {
90                  mask_image.at<float>(y, x) = 1.0;
91                  mask_image.at<float>(EDGE_M_1 - y, x) = 1.0;
92                  mask_image.at<float>(y, EDGE_M_1 - x) = 1.0;
93                  mask_image.at<float>(EDGE_M_1 - y, EDGE_M_1 - x) = 1.0;
94              }
95          }
96      }
97
98      // Initialize resources for frequency domain filtering.
99      cv::Mat planes[2] = {cv::Mat_<float>(process_image)
100     , cv::Mat::zeros(process_image.size(), CV_32F)};
```

```
101     cv::Mat complex_image;
102     cv::merge(planes, 2, complex_image);
103
104     // Compute the DFT.
105     cv::dft(complex_image, complex_image, cv::DFT_COMPLEX_OUTPUT);
106
107     // Split into real and imaginary parts.
108     cv::split(complex_image, planes);
109     // Multiply both parts individually with the mask.
110     planes[0] = planes[0].mul(mask_image);
111     planes[1] = planes[1].mul(mask_image);
112     // Merge the new real and imaginary parts.
113     cv::merge(planes, 2, complex_image);
114
115     // Compute the inverse DFT.
116     cv::dft(complex_image, complex_image, cv::DFT_INVERSE);
117     cv::split(complex_image, planes);
118     // Get the element-wise magnitude.
119     cv::magnitude(planes[0], planes[1], process_image);
120
121     cv::normalize(process_image, process_image, 0.0, 255.0, CV_MINMAX);
122     process_image.convertTo(process_image, CV_8U);
123
124     // Compute the threshold image.
125     cv::adaptiveThreshold(process_image, threshold_image, 255.0
126     , cv::ADAPTIVE_THRESH_GAUSSIAN_C, cv::THRESH_BINARY_INV, 49, 10.0);
127     // Erode the image.
128     cv::erode(threshold_image, threshold_image, erosion_kernel);
129
130     // Determine the contours in the threshold image.
131     cv::findContours(threshold_image, contours, hierarchy, cv::
            RETR_EXTERNAL
132     , cv::CHAIN_APPROX_SIMPLE, cv::Point(0, 0));
133
134     cv::drawContours(user_image, contours, -1, cv::Scalar(0, 0, 255), 2,
            8, hierarchy);
135
136     // Determine the centre for each contour detected (using bounding
            boxes).
137     for (size_t i = 0; i < contours.size(); i++) {
138         cv::Rect bound_rect = cv::boundingRect(contours[i]);
139         ctr_centres.push_back(cv::Point2d(bound_rect.x + (bound_rect.
                width / 2)
140         , bound_rect.y + (bound_rect.height / 2)));
141     }
142 }
143
144 void EggIdentify::run(void) {
145
146     ctr_centres.clear();
147     determine_contour_centres();
148 }
```

A-2-3 Schistoscope.cpp

```
#include <iostream>

#include <opencv2/core.hpp>
#include "opencv2/highgui.hpp"

#include "util/eggidentify.h"

int main(int argc, char const *argv[])
{
    EggIdentify EggId = EggIdentify();

    EggId.capture_image();
    EggId.run();

    // EggId.show_img(EggIdentify::RAW_IMAGE);

    cv::waitKey(0);

    return 0;
}
```

Bibliography

[1] Centers for Disease Control and Prevention, "Schistosomiasis." https://www.cdc.gov/parasites/schistosomiasis/, 2019.

[2] R. Bergquist, M. V. Johansen, and J. Utzinger, "Diagnostic dilemmas in helminthology: what tools to use and when?," *Trends in Parasitology*, vol. 25, pp. 151–156, Apr 2009.

[3] E. Linder, A. Grote, S. Varjo, N. Linder, M. Lebbad, M. Lundin, V. Diwan, J. Hannuksela, and J. Lundin, "On-chip imaging of schistosoma haematobium eggs in urine for diagnosis by computer vision," *PLOS Neglected Tropical Diseases*, vol. 7, pp. 1–9, 12 2013.

[4] A. Maia Chagas, L. L. Prieto-Godino, A. B. Arrenberg, and T. Baden, "The €100 lab: A 3d-printable open-source platform for fluorescence microscopy, optogenetics, and accurate temperature control during behaviour of zebrafish, drosophila, and caenorhabditis elegans," *PLOS Biology*, vol. 15, pp. 1–21, 07 2017.

[5] T. Aidukas, R. Eckert, A. R. Harvey, L. Waller, and P. C. Konda, "Low-cost, sub-micron resolution, wide-field computational microscopy using opensource hardware," *Scientific Reports*, vol. 9, no. 1, p. 7457, 2019.

[6] ZEISS, Education in Microscopy and Digital Imaging, "Numerical Aperture and Resolution." http://zeiss-campus.magnet.fsu.edu/articles/basics/resolution.html.

[7] "Raspberry pi camera module documentation." https://www.raspberrypi.org/documentation/hardware/camera/.

[8] Centers for Disease Control and Prevention, "Neglected tropical diseases." https://www.cdc.gov/globalhealth/ntd/diseases/index.html, 2019.

[9] D. G. Colley, A. L. Bustinduy, W. E. Secor, and C. H. King, "Human schistosomiasis," *The Lancet*, vol. 383, pp. 2253–2264, Jun 2014.

[10] G. . D. Collaborators, I. Incidence, and Prevalence, "Global, regional, and national incidence, prevalence, and years lived with disability for 310 diseases and injuries, 1990-2015: a systematic analysis for the global burden of disease study 2015," *Lancet (London, England)*, vol. 388, pp. 1545–1602, Oct 2016.

[11] World Health Organization, "Schistosomiasis fact sheet." https://www.who.int/news-room/fact-sheets/detail/schistosomiasis, 2019.

[12] C. H. King, R. F. Sturrock, H. C. Kariuki, and J. Hamburger, "Transmission control for schistosomiasis - why it matters now," *Trends in Parasitology*, vol. 22, pp. 575–582, Dec 2006.

[13] S. A.-L. Thétiot-Laurent, J. Boissier, A. Robert, and B. Meunier, "Schistosomiasis chemotherapy," *Angewandte Chemie International Edition*, vol. 52, no. 31, pp. 7936–7956, 2013.

[14] G. . M. Collaborators and C. of Death, "Global, regional, and national life expectancy, all-cause mortality, and cause-specific mortality for 249 causes of death, 1980-2015: a systematic analysis for the global burden of disease study 2015," *Lancet (London, England)*, vol. 388, pp. 1459–1544, Oct 2016.

[15] WHO/Department of control of neglected tropical diseases, "Schistosomiasis and soil-transmitted helminthiases: number of people treated in 2016," 2017.

[16] L. Le and M. H. Hsieh, "Diagnosing urogenital schistosomiasis: Dealing with diminishing returns," *Trends in Parasitology*, vol. 33, pp. 378–387, May 2017.

[17] WHO, "Manual of Basic Techniques for a Health Laboratory, 2e," pp. 249–251, 2003.

[18] Institute of Medicine, "Malaria: Obstacles and Opportunities," p. 75, 1991.

[19] W. P. O'Meara, M. Barcus, C. Wongsrichanalai, S. Muth, J. D. Maguire, R. G. Jordan, W. R. Prescott, and F. E. McKenzie, "Reader technique as a source of variability in determining malaria parasite density by microscopy," *Malaria journal*, vol. 5, pp. 118–118, Dec 2006.

[20] M. G. Cavalcanti, L. F. Silva, R. H. S. Peralta, M. G. M. Barreto, and J. M. Peralta, "Schistosomiasis in areas of low endemicity: a new era in diagnosis," *Trends in Parasitology*, vol. 29, pp. 75–82, Feb 2013.

[21] M. Chand, P. Chiodini, and M. Doenhoff, "Development of a new assay for the diagnosis of schistosomiasis, using cercarial antigens," *Transactions of The Royal Society of Tropical Medicine and Hygiene*, vol. 104, pp. 255–258, 04 2010.

[22] R. R. F. Candido, T. G. St Pierre, A. L. Morassutti, C. Graeff-Teixeira, and M. K. Jones, "Eggs and magnetism: New approaches for schistosomiasis diagnosis," *Trends in Parasitology*, vol. 34, pp. 267–271, Apr 2018.

[23] R. R. Candido, V. Favero, M. Duke, S. Karl, L. Gutiérrez, R. C. Woodward, C. Graeff-Teixeira, M. K. Jones, and T. G. S. Pierre, "The affinity of magnetic microspheres for schistosoma eggs," *International Journal for Parasitology*, vol. 45, no. 1, pp. 43 – 50, 2015.

[24] J. C. Sousa-Figueiredo, M. Betson, N. B. Kabatereine, and J. R. Stothard, "The urine circulating cathodic antigen (cca) dipstick: A valid substitute for microscopy for mapping and point-of-care diagnosis of intestinal schistosomiasis," *PLOS Neglected Tropical Diseases*, vol. 7, pp. 1–11, 01 2013.

[25] O. F. Bamgbola, "Urinary schistosomiasis," *Pediatric Nephrology*, vol. 29, pp. 2113–2120, Nov 2014.

[26] J. Rajchgot, J. T. Coulibaly, J. Keiser, J. Utzinger, N. C. Lo, M. K. Mondry, J. R. Andrews, and I. I. Bogoch, "Mobile-phone and handheld microscopy for neglected tropical diseases," *PLOS Neglected Tropical Diseases*, vol. 11, pp. 1–4, 07 2017.

[27] T. E. Agbana, J.-C. Diehl, F. van Pul, S. M. Khan, V. Patlan, M. Verhaegen, and G. Vdovin, "Imaging & identification of malaria parasites using cellphone microscope with a ball lens," *PLOS ONE*, vol. 13, pp. 1–13, 10 2018.

[28] M. Poostchi, K. Silamut, R. J. Maude, S. Jaeger, and G. Thoma, "Image analysis and machine learning for detecting malaria," *Translational research : the journal of laboratory and clinical medicine*, vol. 194, pp. 36–55, Apr 2018.

[29] D. Rollinson, J. R. Stothard, and V. R. Southgate, "Interactions between intermediate snail hosts of the genus bulinus and schistosomes of the schistosoma haematobium group," *Parasitology*, vol. 123, pp. 245–260, Nov 2001.

[30] M. G. Cavalcanti and J. M. Peralta, "Schistosomiasis – updating technologies and diagnostic approaches in surveillance strategies and clinical management," in *An Overview of Tropical Diseases* (A. Samie, ed.), ch. 7, Rijeka: IntechOpen, 2015.

[31] O. A. Ibironke, A. E. Phillips, A. Garba, S. M. Lamine, and C. Shiff, "Diagnosis of schistosoma haematobium by detection of specific dna fragments from filtered urine samples," *The American journal of tropical medicine and hygiene*, vol. 84, pp. 998–1001, Jun 2011. 21633040[pmid].

[32] H. S. Hutchison, "The pathology of bilharziasis," *The American journal of pathology*, vol. 4, pp. 1–16.11, Jan 1928. 19969774[pmid].

[33] D. G. Bostwick, "7 - urine cytology," in *Urologic Surgical Pathology (Fourth Edition)* (L. Cheng, G. T. MacLennan, and D. G. Bostwick, eds.), pp. 322 – 357.e7, Philadelphia: Content Repository Only!, fourth edition ed., 2020.

[34] A. W. Cheever, S. W. Young, and A. Shehata, "Calcification of Schistosoma haematobium eggs: Relation of radiologically demonstrable calcification to eggs in tissues and passage of eggs in urine," *Transactions of The Royal Society of Tropical Medicine and Hygiene*, vol. 69, pp. 410–414, 01 1975.

[35] P. A. Peters, A. A. Mahmoud, K. S. Warren, J. H. Ouma, and T. K. Siongok, "Field studies of a rapid, accurate means of quantifying schistosoma haematobium eggs in urine samples," *Bulletin of the World Health Organization*, vol. 54, no. 2, pp. 159–162, 1976. 1088097[pmid].

[36] M. V. D'Ambrosio, M. Bakalar, S. Bennuru, C. Reber, A. Skandarajah, L. Nilsson, N. Switz, J. Kamgno, S. Pion, M. Boussinesq, T. B. Nutman, and D. A. Fletcher, "Point-of-care quantification of blood-borne filarial parasites with a mobile phone microscope," *Science Translational Medicine*, vol. 7, no. 286, pp. 286re4–286re4, 2015.

[37] N. A. Switz, M. V. D'Ambrosio, and D. A. Fletcher, "Low-cost mobile phone microscopy with a reversed mobile phone camera lens," *PLOS ONE*, vol. 9, pp. 1–7, 05 2014.

[38] I. I. Bogoch, J. R. Andrews, B. Speich, J. Utzinger, S. M. Ame, S. M. Ali, and J. Keiser, "Mobile phone microscopy for the diagnosis of soil-transmitted helminth infections: a proof-of-concept study," *The American journal of tropical medicine and hygiene*, vol. 88, pp. 626–629, Apr 2013. 23478580[pmid].

[39] J. S. Cybulski, J. Clements, and M. Prakash, "Foldscope: Origami-based paper microscope," *PLOS ONE*, vol. 9, pp. 1–11, 06 2014.

[40] S. J. Sowerby, J. A. Crump, M. C. Johnstone, K. L. Krause, and P. C. Hill, "Smartphone microscopy of parasite eggs accumulated into a single field of view," *The American journal of tropical medicine and hygiene*, vol. 94, pp. 227–230, Jan 2016. 26572870[pmid].

[41] J. T. Coulibaly, M. Ouattara, J. Keiser, B. Bonfoh, E. K. N'Goran, J. R. Andrews, and I. I. Bogoch, "Evaluation of malaria diagnoses using a handheld light microscope in a community-based setting in rural côte d'ivoire," *The American journal of tropical medicine and hygiene*, vol. 95, pp. 831–834, Oct 2016. 27527637[pmid].

[42] R. A. A. Campbell, R. W. Eifert, and G. C. Turner, "Openstage: a low-cost motorized microscope stage with sub-micron positioning accuracy," *PloS one*, vol. 9, pp. e88977–e88977, Feb 2014. 24586468[pmid].

[43] Z. Grier, M. F. Soddu, N. Kenyatta, S. A. Odame, J. Sanders, L. Wright, and F. Anselmi, "A low-cost do-it-yourself microscope kit for hands-on science education," in *Optics Education and Outreach V* (G. G. Gregory, ed.), vol. 10741, pp. 133 – 148, International Society for Optics and Photonics, SPIE, 2018.

[44] "Raspberry pi." https://www.raspberrypi.org/.

[45] Alasdair Allan, "Benchmarking Machine Learning on the New Raspberry Pi 4, Model B." https://www.hackster.io/news/benchmarking-machine-learning-on-the-new-raspberry-pi-4-model-b-88db9304ce4.

[46] nVIDIA Developer, "Jetson Nano: Deep Learning Inference Benchmarks." https://developer.nvidia.com/embedded/jetson-nano-dl-inference-benchmarks.

[47] R. C. Gonzalez and R. E. Woods, *Digital Image Processing (3rd Edition)*. USA: Prentice-Hall, Inc., 2006.

[48] L. Taylor and G. Nitschke, "Improving deep learning with generic data augmentation," in *2018 IEEE Symposium Series on Computational Intelligence (SSCI)*, pp. 1542–1547, Nov 2018.

[49] B. E. Boser, I. M. Guyon, and V. N. Vapnik, "A training algorithm for optimal margin classifiers," in *Proceedings of the Fifth Annual Workshop on Computational Learning Theory*, COLT '92, (New York, NY, USA), p. 144–152, Association for Computing Machinery, 1992.

[50] C. Cortes and V. Vapnik, "Support-vector networks," *Machine Learning*, vol. 20, no. 3, pp. 273–297, 1995.

[51] F. Pedregosa, G. Varoquaux, A. Gramfort, V. Michel, B. Thirion, O. Grisel, M. Blondel, P. Prettenhofer, R. Weiss, V. Dubourg, J. Vanderplas, A. Passos, D. Cournapeau, M. Brucher, M. Perrot, and E. Duchesnay, "Scikit-learn: Machine learning in Python," *Journal of Machine Learning Research*, vol. 12, pp. 2825–2830, 2011.

[52] G. Bradski, "The OpenCV Library," *Dr. Dobb's Journal of Software Tools*, 2000.

[53] "London Declaration on Neglected Tropical Diseases." https://www.who.int/neglected_diseases/London_Declaration_NTDs.pdf, 2012.